The Most Compact Bright Radio-loud AGNs. II.
VLBA Observations of 10 Sources at 43 and 86 GHz

X.-P. Cheng[1,2], T. An[1,3], X.-Y. Hong[1,2,3], J. Yang[1,4], P. Mohan[1], K. I. Kellermann[5], M. L. Lister[6], S. Frey[7],
W. Zhao[1], Z.-L. Zhang[1], X.-C. Wu[1], X.-F. Li[1,2], and Y.-K. Zhang[1,2]

[1] Shanghai Astronomical Observatory, Chinese Academy of Sciences, Shanghai 200030, People's Republic of China; antao@shao.ac.cn
[2] University of Chinese Academy of Sciences, 19A Yuquanlu, Beijing 100049, People's Republic of China
[3] Key Laboratory of Radio Astronomy, Chinese Academy of Sciences, 210008 Nanjing, People's Republic of China
[4] Department of Earth and Space Sciences, Chalmers University of Technology, Onsala Space Observatory, SE-43992 Onsala, Sweden
[5] National Radio Astronomy Observatory, 520 Edgemont Road, Charlottesville, VA 22903, USA
[6] Department of Physics, Purdue University, 525 Northwestern Avenue, West Lafayette, IN 47907, USA
[7] Konkoly Observatory, MTA Research Centre for Astronomy and Earth Sciences, Konkoly Thege Miklós út 15-17, H-1121 Budapest, Hungary

Abstract

Radio-loud active galactic nuclei (AGNs), hosting powerful relativistic jet outflows, provide an excellent laboratory for studying jet physics. Very long baseline interferometry (VLBI) enables high-resolution imaging on milli-arcsecond (mas) and sub-mas scales, making it a powerful tool to explore the inner jet structure, shedding light on the formation, acceleration, and collimation of AGN jets. In this paper, we present Very Long Baseline Array observations of 10 radio-loud AGNs at 43 and 86 GHz that were selected from the *Planck* catalog of compact sources and are among the brightest in published VLBI images at and below 15 GHz. The image noise levels in our observations are typically 0.3 and 1.5 mJy beam^{-1} at 43 and 86 GHz, respectively. Compared with the VLBI data observed at lower frequencies from the literature, our observations with higher resolutions (with the highest resolution being up to 0.07 mas at 86 GHz and 0.18 mas at 43 GHz) and at higher frequencies detected new jet components at sub-parsec scales, offering valuable data for studies of the physical properties of the innermost jets. These include the compactness factor of the radio structure (the ratio of core flux density to total flux density), and core brightness temperature (T_b). In all these sources, the compact core accounts for a significant fraction (>60%) of the total flux density. Their correlated flux density at the longest baselines is higher than 0.16 Jy. The compactness of these sources make them good phase calibrators of millimeter-wavelength ground-based and space VLBI.

Key words: galaxies: active – galaxies: jets – quasars: general – surveys – techniques: high angular resolution

1. Introduction

Radio-loud active galactic nuclei (AGNs) host prominent relativistic jets of magnetized plasma, which may extend far beyond the host galaxy, and hence are good laboratories to study AGN phenomena and jet physics. General relativistic magneto-hydrodynamic simulations suggest a jet–disk connection, mediated by the magnetic field (Narayan 2005; McKinney et al. 2012; Tchekhovskoy et al. 2012). Observational evidence of disk–jet coupling has been acquired in AGN (e.g., Chatterjee et al. 2009; An et al. 2013) and in black hole-accretion X-ray binaries (Plotkin et al. 2017), but there are still many open questions related to the creation and collimation of relativistic jets (Komissarov et al. 2007). Imaging the region near the start of the jet on sub-parsec scales can shed light on the mechanism of acceleration and collimation of jet flow (Doeleman et al. 2012). The brightness temperature of the core and estimated Doppler factors of the parsec-scale jet provide supplementary clues for jet kinematic parameters and energetics.

Very Long Baseline Interferometry (VLBI) makes high-resolution imaging of the fine structure possible. A recent milestone was passed using the space radio telescope on board the *RadioAstron* satellite with ground-based telescopes that resulted in a high angular resolution of 7 μas (Kardashev et al. 2013). Synchrotron emission is dominant in AGN jets and originates from the most compact region in the vicinity of the jet origin, i.e., the radio core. Since synchrotron emission of the core is mostly self-absorbed at long centimeter wavelengths (Kellermann & Pauliny-Toth 1969), millimeter-wavelength VLBI is best suited to exploring the mysteries of AGN jets. The first single-baseline interference fringes at 89 GHz (3.4 mm-wavelength) were detected in 3C 84 in 1981 (Readhead et al. 1983). Since then, several millimeter-wavelength VLBI surveys of AGNs have been conducted at 86 GHz (Beasley et al. 1997; Lonsdale et al. 1998; Rantakyrö et al. 1998; Lobanov et al. 2000; Lee et al. 2008, 2016), and 43 GHz (Krichbaum & Witzel 1992; Lister 2001; Marscher et al. 2002; Lanyi et al. 2010; Petrov et al. 2012). These surveys imaged the inner sub-parsec jet with unprecedented resolution, and greatly improved our understanding of the jet physics and how it is related to the jet launching, acceleration and collimation, and the role of the supermassive black hole in those processes. A total of 121 AGNs have been successfully imaged at 86 GHz. Other large VLBI surveys of AGNs (e.g., Kellermann et al. 2004; Helmboldt et al. 2007; Petrov et al. 2008; Lister et al. 2009) were made at lower frequencies, providing radio images of jets on scales of millarcseconds (mas) to tens of mas.

To further increase the maximum baseline length, so as to improve the angular resolution, space VLBI (SVLBI) has been developed, involving the deployment of radio telescopes on Earth-orbiting spacecraft (Burke 1984). Such efforts led to two successful SVLBI missions, i.e., the Japan-led VLBI Space Observatory Programme (VSOP, Hirabayashi et al. 1998) and the Russia-led *RadioAstron* (Kardashev et al. 2013). A step

forward was taken by the Shanghai Astronomical Observatory (SHAO) of the Chinese Academy of Sciences (CAS), which has proposed a Space Millimeter-wavelength VLBI array (SMVA) program involving two satellites each carrying a 10 m radio telescope. The SMVA is planed to be operational at up to 43 GHz frequency and will conduct joint observations together with ground-based VLBI stations to provide high-resolution and high-sensitivity images (Hong et al. 2014). The apogee height of the two satellites will be approximately 60,000 km (∼5 times the diameter of the Earth), thus, it will be able to achieve very high angular resolutions of ∼20 μas at a peak frequency of 43 GHz. Using two satellites will allow excellent (u, v) coverage on space–ground baselines to be obtained. With an improved resolution and better imaging capability than ever, the SMVA program is expected to pave the way for future space-based millimeter (mm) and sub-millimeter (sub-mm) VLBI arrays.

In order to prepare for the SMVA program, we initiated a VLBI observing program with the Very Long Baseline Array (VLBA) at high (43 and 86 GHz) frequencies. The whole sample (Paper I: An et al. 2014) contains 134 bright AGNs that are selected from the *Planck* catalog of compact sources (PCCS, Planck Collaboration et al. 2011) and the *Wilkinson Microwave Anisotropy Probe* (*WMAP*) catalog (Chen & Wright 2009; Geréb & Frey 2011; Gold et al. 2011). Details on the sample selection criteria are given in Paper I and also briefly in Section 2.1. The technical objective of the observing program is to enlarge the sample sizes of AGNs that are suitable for space mm-wavelength VLBI. The science objective is to reveal the sub-parsec emission structure of the AGN jets, and collect crucial information for studies of jet collimation and acceleration. The observations were divided into two sessions based on their different primary science motivations and observation setups. For Session I, 10 bright high-declination sources were selected to be observed at both 43 and 86 GHz with long integration times (a total of 80 minutes on each source) and good (u, v) coverage, in order to acquire good images for further detailed study of the inner jet. The 10 targets for high-sensitivity imaging were selected in the context of the sparse high-frequency VLBI imaging information about these objects in the existing literature. In Session II, the remaining 124 sources were observed in snapshot mode with relatively shorter integration times (two to four scans, each seven minutes) at 43 GHz. The main purpose was to check whether these sources are detectable with VLBA at this frequency. The results from the Session I observations are presented in this paper. The forthcoming Paper III (X.-P. Cheng et al. 2018, in preparation) will present the survey results and images of the remaining 124 AGNs observed in Session II. The statistics of the parsec-scale jet properties, e.g., the brightness temperature and radio–γ-ray luminosity correlation, will be discussed in Paper III, based on the entire sample of 134 sources plus other data from the literature.

As 86 GHz VLBI imaging surveys are relatively rare to date, the new high-sensitivity high-resolution data presented here will be of additional value for, e.g., identifying good phase calibrators for Event Horizon Telescope (EHT; Doeleman et al. 2009) observations. They will also supplement shallower but more extensive all-sky surveys for potential calibrators, establishing synergy with other surveys with relatively lower resolutions, e.g., the KVN and VERA array AGN survey (Niinuma et al. 2014).

The current paper presents the observational results of the brightest 10 sources observed in Session I. The paper is structured as follows. In Section 2, the sample selection, observation, and data reduction details are given. In Section 3, the imaging results are presented and the morphological properties of individual sources are discussed. In Section 4, the main results of the paper are summarized. Throughout this paper, the spectral index is defined by the convention $S \propto \nu^\alpha$, and a standard cosmological model with $H_0 = 73 \, \mathrm{km \, s^{-1} \, Mpc^{-1}}$, $\Omega_M = 0.27$ and $\Omega_\Lambda = 0.73$ is adopted.

2. VLBA Observations and Data Reduction

2.1. Target Selection

A high-resolution high-frequency VLBI imaging survey of bright and compact AGNs is necessary for the preparation of future mm-wavelength space VLBI campaigns (e.g., SMVA). For this purpose, we observed with the VLBA a sample of bright AGNs that did not previously have high-sensitivity VLBI images at the frequency of 43 GHz. The sources in our survey were selected by cross-matching archival ground-based VLBI images (e.g., Ma et al. 2013) with the *WMAP* catalog (Chen et al. 2013) and *Planck* catalog (Planck Collaboration et al. 2011) with the following selection criteria: (1) J2000 declination is $> -30°$, as below this declination, it is difficult for the VLBA to create good images; (2) the sources are not included in previous 43 GHz VLBI catalogs (Lister 2001; Marscher et al. 2002); and (3) the radio emission is dominated by a prominent core in low-frequency VLBI images whose expected flux density at 43 GHz is higher than 0.3 Jy. Combining the above three catalogs and selection criteria, we obtained a sample of 134 bright AGNs, including: 105 quasars, 17 BL Lac objects, 6 radio galaxies, and 6 objects with no optical identification.

We observed all these 134 AGNs with the VLBA from 2014 to 2016. The observations were divided into two sessions with different objectives, as mentioned in Section 1: Session I—to acquire high-sensitivity high-resolution images of the 10 brightest AGNs selected from our whole sample; and Session II—to carry out an imaging survey at 43 GHz including the remaining 124 sources.

The 10 AGNs contained in Session I are selected with even tighter criteria:

1. J2000 declination is $> +30°$ for a good (u, v) coverage;
2. The candidates show a compact core–jet morphology in 15 GHz VLBA images (Lister et al. 2009); and
3. The correlated 43 GHz flux density on the shortest baseline (column 8 in Table 1) is higher than 0.65 Jy (with the exception of 0529+483, which has a total flux density of 2.1 Jy at 15 GHz but a lower 43 GHz flux density of 0.35 Jy).

The main purpose was to image the compact jet structure with a parsec or sub-parsec spatial resolution (a typical angular resolution of 0.2 mas from the observations corresponds to a physical size of 0.4 pc at $z = 0.1$ and 1.6 pc at $z = 1$). These observations offer unique data for studying the structure of the inner sub-parsec-scale jet, high-frequency physical properties of the jet emission, e.g., the brightness temperature of the core, and the correlation between the high-energy gamma-ray (which

Table 1
Source Information

IAU Name (1)	z (2)	ID (3)	R.A. (J2000) (4)	Decl. (J2000) (5)	S_{44} (Jy) (6)	S_{15} (Jy) (7)	S_8 (Jy) (8)
0202+319 (J0205+3212)	1.466	QSO	02 05 04.92536	+32 12 30.0954	1.82	2.41	1.50
0529+483 (J0533+4822)	1.162	QSO	05 33 15.86578	+48 22 52.8076	1.12	1.27	1.47
1030+415 (J1033+4116)	1.1185	QSO	10 33 03.70786	+41 16 06.2329	1.86	2.52	1.09
1128+385 (J1130+3815)	1.7405	QSO	11 30 53.28261	+38 15 18.5469	0.96	1.43	1.06
1418+546 (J1419+5423)	0.1526	BL Lac	14 19 46.59740	+54 23 14.7871	0.64	1.01	0.81
1823+568 (J1824+5651)	0.664	BL Lac	18 24 07.06837	+56 51 01.4908	1.39	1.25	1.16
1828+487 (J1829+4844)	0.692	QSO	18 29 31.78093	+48 44 46.1613	2.96	2.20	1.83
1928+738 (J1927+7358)	0.3021	QSO	19 27 48.49516	+73 58 01.5698	5.01	4.51	3.70
1954+513 (J1955+5131)	1.22	QSO	19 55 42.73826	+51 31 48.5461	0.92	0.94	1.40
2201+315 (J2203+3145)	0.295	QSO	22 03 14.97578	+31 45 38.2699	2.82	3.18	1.76

Note. (1) Source name; (2) redshift; (3) classification; (4) R.A. (J2000); (5) decl. (J2000); (6) flux density at 44 GHz obtained from *Planck* (Planck Collaboration et al. 2011); (7) integrated flux density at 15 GHz obtained from VLBA (Lister et al. 2013); (8) integrated flux density observed at 8 GHz with the VLBA (Pushkarev & Kovalev 2012).

Table 2
Observation Logs

Code (1)	ν (GHz) (2)	Date (yyyy mm dd) (3)	Target Sources (4)	Calibrators (5)	Telescopes (6)
BA111A	43	2014 Nov 21	0202+319, 0529+483	3C 84, 0355+508	VLBA
BA111B	43	2015 Mar 08	1030+415, 1128+385, 1418+546	3C 273, 3C 279	VLBA
BA111C	43	2015 Jan 10	1823+568, 1828+487 1928+738, 1954+513, 2201+315	3C 279, 3C 453.3	VLBA
BA111D	86	2014 Nov 30	0202+319, 0529+483	3C 84, 0355+508	VLBA(−SC HN)
BA111E	86	2014 Nov 29	1030+415, 1128+385, 1418+546	3C 273, 3C 279	VLBA(−SC HN)
BA111F	86	2016 May 06	1823+568, 1828+487 1928+738, 1954+513, 2201+315	3C 279, 3C 453.3	VLBA(−SC HN BR)

Note. (1) Project codes of the sub-sessions; (2) observing frequency; (3) date of observation; (4) target sources; (5) fringe-finding calibrators; (6) telescopes involved in the observations (telescopes that were not used in individual observations are shown in brackets).

is thought to arise from the parsec-scale jet) and radio emission. The observations can also be used as a reference epoch for future high-resolution jet proper motion studies at these frequencies. Table 1 summarizes general information about the 10 sources.

2.2. Observations

The right ascensions of the 10 target sources were spread between R.A. = 02^h and R.A. = 22^h. In order to optimize the (u, v) coverage of each source, we divided them into three groups. The observations at 43 and 86 GHz were carried out in six different epochs from 2014 November 21 to 2016 May 6 (project codes of sub-sessions BA111A to BA111F; PI: T. An). Originally, in the observing proposal, we asked for nearly simultaneous observations at 43 and 86 GHz to facilitate spectral studies, but due to scheduling constraints (the 86 GHz experiments were dynamically scheduled based on good weather conditions) the observations were not performed simultaneously by the VLBA. Because of dynamical scheduling constraints and the more stringent weather requirements at 86 GHz, the two frequencies were observed in separate sessions, rather than simultaneously. Full polarization measurements were not possible due to the limited parallactic angle coverage associated with the short session durations (3–8 hours). Table 2 summarizes the observation setups. All 10

VLBA stations were used for the 43 GHz observations. All the antennas except Saint Croix (SC) and Hancock (HN), which do not have an 86 GHz receiver, were used for the 86 GHz observations, except the antenna Brewster (BR) was not used for the last epoch (BA111F) due to the scheduled maintenance. Millimeter-wavelength VLBI observations are easily affected by tropospheric fluctuations, so the observing periods were carefully chosen to have exceptionally favorable weather conditions. At the beginning and the end of each observation, there was a calibrator of bright quasars: 3C 84, 3C 273, 3C 279, 3C 454.3, or 0355+508 (4C +50.11). All the data were recorded with 2-bit sampling at an aggregate data rate of 2 Gbps, on eight intermediate frequency (IF) channels of 32 MHz each. On average, each source was observed for five 16-minute scans, which were interlaced with other sources to giveoptimal (u, v) coverage. Figure 1 displays typical 43 GHz (u, v) coverage for the lowest-declination source, 0202+319 and the highest-declination one, 1928+738 among this sample. The raw data were correlated using the DiFX software correlator (Deller et al. 2007, 2011) at Socorro, NM, with a 2 s averaging time, 128 channels per IF, and uniform weighting.

2.3. Data Reduction

The data reduction was performed using the NRAO Astronomical Imaging Processing Software (AIPS) package
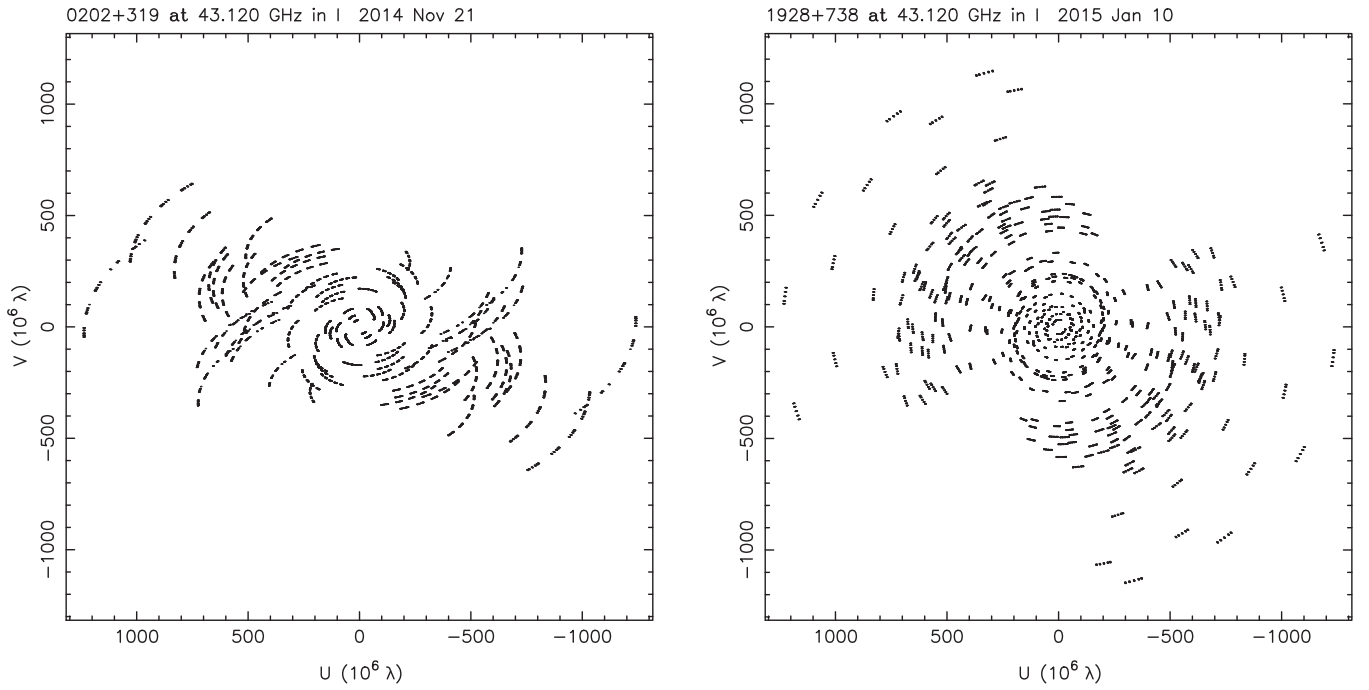
Figure 1. (u, v) coverages at 43 GHz of the lowest- and highest-declination sources among the sample. The labels on the x- and y-axes are in units of 10^6 times the observing wavelength λ.

(Greisen 2003) following the standard procedure described in the AIPS cookbook. We first imported the data into AIPS using the task FITLD, and inspected the data quality. A handful of bad datapoints that were mostly caused by abnormally high system temperatures were flagged before further data processing. The central station Pie Town (PT) was chosen as the reference antenna in the calibration process. Fort Davis (FD) was used as an alternative when PT was not available. We ran the task ACCOR to remove sampler bias caused by errors in sampler thresholds. Then, we used the AIPS task APCAL to make the initial amplitude calibration for each intermediate frequency (IF) channel using system temperature measurements, which were also applied with atmospheric opacity corrections and gain curves measured at each station during the observations. After a priori amplitude calibration of the visibility data, we carried out fringe-fitting using a short scan (generally 1 minute) of the fringe-finding calibrator data to measure the single-band delay offsets across different IFs, and applied the resulting solutions to all the sources. A signal-to-noise ratio threshold of 5 was set to avoid false detections in fringe-fitting. After removing instrumental phase offsets across each IF, we used global fringe-fitting by combining all IFs to determine the frequency- and time-dependent phase errors at each antenna and removed them from the data. After global fringe-fitting, the solutions were applied to each individual source by linear phase connection using fringe rates to resolve phase ambiguities. In the final step, we used the task BPASS to calibrate the bandpass shapes by fitting a short scan of a bright calibrator. After the above calibrations were applied, single-source data sets in FITS format were exported into the Caltech Difmap imaging program (Shepherd 1997). Self-calibration was performed in Difmap to remove residual phase errors. The final images were produced after a few further iterations of deconvolution, phase, and amplitude self-calibration. In order to quantify the brightness distribution of the core and jet

components, we used the task MODELFIT to fit the visibility data in Difmap. An elliptical Gaussian model was used to fit the brightest component, which is commonly identified as the AGN core, and circular Gaussian models were used to fit jet components.

3. Analysis and Results

3.1. Imaging Results

Figures 2–11 show the total intensity images of the 10 sources at 43 and 86 GHz obtained from the present paper and lower-frequency images from the literature. All of the 43 GHz images are characterized by a one-sided core–jet structure. Six sources have a compact jet with an extent of about 1 mas. Another four sources (1823+568, 1928+738, 1954+513, 2201 +315) have jets extending to an angular distance of 2–4 mas. Fifteen GHz VLBA images from the MOJAVE (Monitoring Of Jets in AGNs with VLBA Experiments, Lister et al. 2009) program[8] observed at the recent epochs were used for comparison of the inner jet structure with the 43 and 86 GHz ones. Archival 1.4 GHz images were adopted to show the extended jet structure on a projected size of tens to hundreds of parsecs. When 1.4 GHz images were not available, 2.3 and 5 GHz archival images were used instead. Table 3 lists the image parameters at each frequency, including the integrated flux density S_{tot}, peak specific density S_{peak}, restoring beam (major axis length B_{maj}, minor axis length B_{min}, position angle of the major axis θ), and the rms noise level. The restoring beam is about 0.5 mas × 0.2 mas in the 43 GHz images, and 0.25 mas × 0.1 mas in the 86 GHz images. The typical rms noise in the images is 0.3 mJy beam^{-1} and 1.5 mJy beam^{-1} at 43 and 86 GHz, respectively. They are approximately two times the expected theoretical thermal noises, which are

---

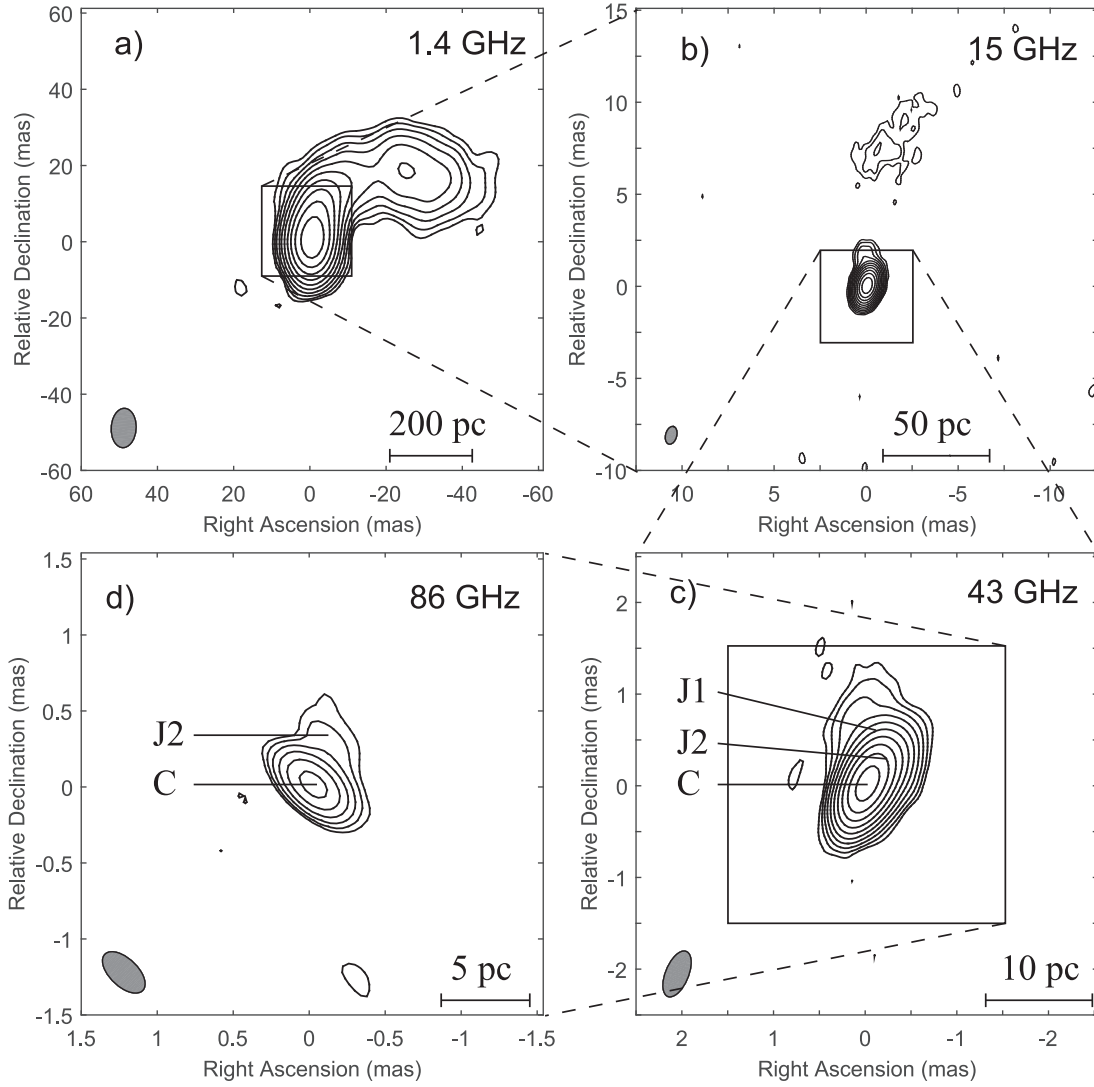[8] http://www.physics.purdue.edu/MOJAVE/

Figure 2. Naturally weighted total intensity VLBI images of 0202+319 at 1.4, 15, 43 GHz, and a uniformly weighted total intensity image at 86 GHz. The image parameters and references are given in Table 3.

0.16 mJy beam^{-1} at 43 GHz and 0.6 mJy beam^{-1} at 86 GHz estimated using the VLBA manual and the online EVN calculator[9]). The difference of a factor of $\sim$2 is partly due to data loss resulting from abnormal system temperature measurements in bad weather conditions, slewing time, and residual calibration errors. The image noises in our observations at 43 GHz and 86 GHz are more than 10 times better than those for earlier large-sample surveys ($\sim$3 mJy beam^{-1} at 43 GHz: e.g., Marscher et al. 2002, and $\sim$15 mJy beam^{-1} at 86 GHz: e.g., Lee et al. 2008). The dynamic ranges of the images (i.e., the ratio of the peak intensity to the rms noise of the image) are between 1000 and 3300 in the 43 GHz images, and between 70 and 330 in the 86 GHz images. The lower dynamic ranges in some images are limited by calibration errors. These values are also about 10 times better than those for previous snapshot observations at the same frequency. The lowest contour represents 3 times the off-source noise level, and the contours are drawn at -1, 1, 2, 4, ..., 2^n times the lowest contour level in Figures 2–11.

3.2. Source Compactness

One of the most important concerns of high-frequency VLBI surveys is the source compactness. In radio-loud AGNs, the core (i.e., optically thick jet base) is usually the most compact and brightest component. The 10 sources in our sample are all blazars and all have prominent cores. In the following analysis of the core and jet properties, we assume the core (labelled-component C in the images) is stationary and used as the reference point. The relative separations of jet components with respect to C were calculated and are shown in Table 4.

The model-fitting parameters are listed in Table 4. The uncertainties on the sizes and core separation of individual Gaussian components in our VLBA images are consistently 15% of the major axis of the core (Hodgson et al. 2017). The uncertainties on fitted flux densities are about 5% and 10% at 43 and 86 GHz, respectively.

In Table 5, columns (3)–(8) show the compactness factors of the sources: the total flux density S_{tot}, the VLBI core flux density S_{core}, the ratio of S_{core}/S_{tot}, the median correlated flux density on the longest baselines derived from the VLBI data S_l, and on the shortest S_s, as well as their ratio S_l/S_s. S_{core} was
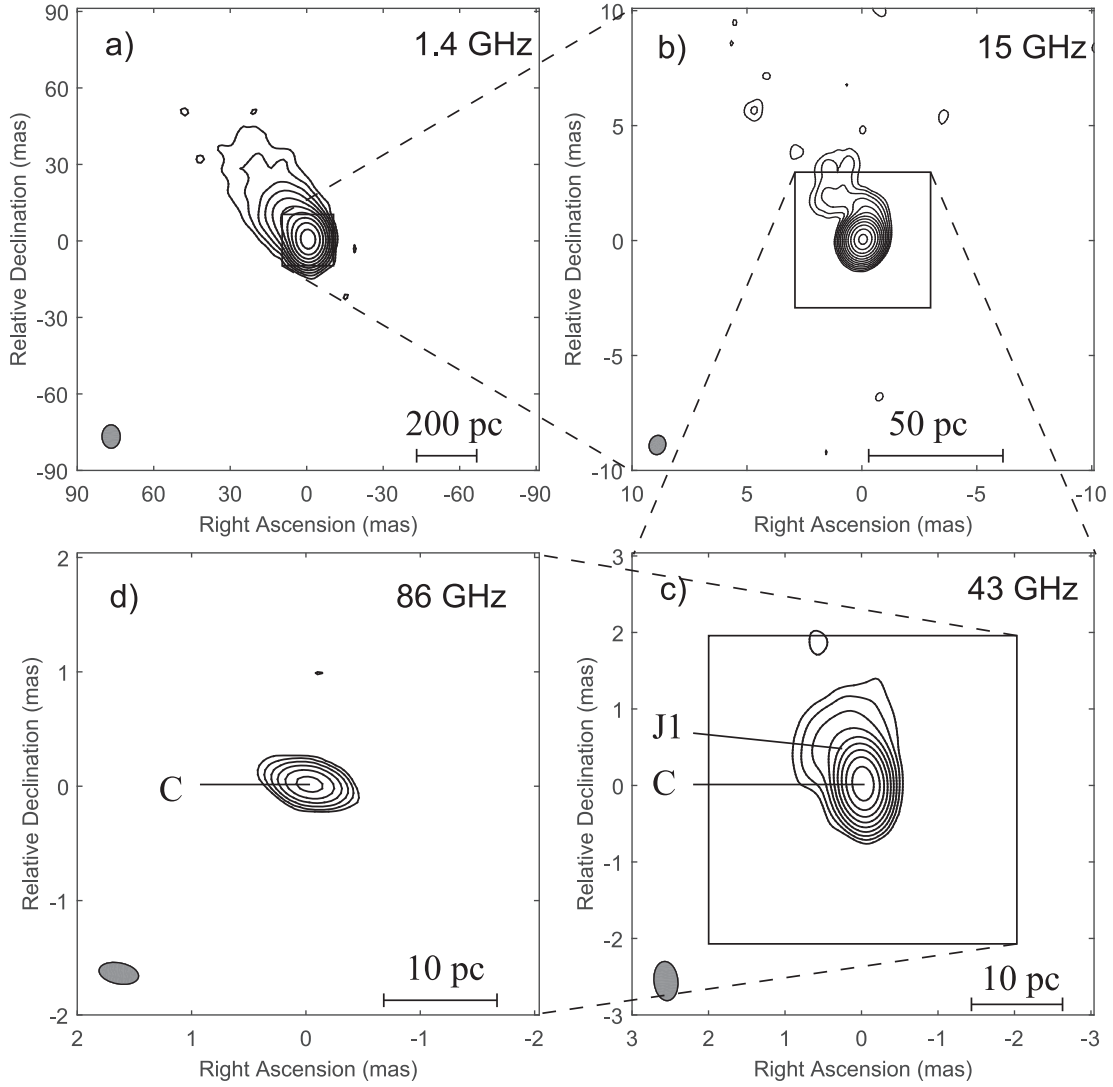
Figure 3. Naturally weighted total intensity VLBI images of 0529+483 at 1.4, 15, 43 GHz, and a uniformly weighted total intensity image at 86 GHz. The image parameters and references are given in Table 3.

obtained from fitting the brightest core component with an elliptical Gaussian model in Difmap. S_{tot} was estimated by integrating the flux density contained in the emission region in the VLBI image. S_s was adopted as the flux density on the shortest baselines; the value of S_l is the flux density measured on the longest baselines in projection on the position angle perpendicular to the core–jet direction.

The structure in the 86 GHz images is either unresolved (with source compactness factors S_{core}/S_{tot} and S_l/S_s close to unity; Table 5) or slightly resolved (S_{core}/S_{tot} and S_l/S_s between 0.5 and 0.8) with the highest resolution being 0.07 mas. More detailed descriptions of the individual source structures are presented in Section 3.2. In general, S_{core}/S_{tot} and S_l/S_s are higher at 86 GHz than at 43 GHz, naturally reflecting that VLBI at 86 GHz detects more compact emission structure that have flatter spectra. Those with compactness factor S_{core}/S_{tot} (43 GHz) higher than 0.7 have typical characteristics of radio-loud AGNs, i.e., high brightness temperatures (Table 6), high core dominance, and apparent superluminal jet motion (see the comments on individual sources in Section 3.2). Relatively lower S_{core}/S_{tot} values are found in 1030+415 (the inner jet showing an S-shape bending,

Section 3.4.3), 1418+546 (Section 3.4.5), and 2201+315 (the kiloparsec-scale structure is of an FR II type, Section 3.4.10). A majority of the sources have $S_l/S_s > 0.5$ at 86 GHz, indicating that they may remain compact even at longer space–ground baselines. Such sources are good candidates for phase calibrators for future mm-wavelength space VLBI.

3.3. Brightness Temperature

Most of the sources show typical blazar characteristics with rapid and high variability in the OVRO 40 m 15 GHz light curves (Richards et al. 2011). From the results of the model fitting, we calculated the brightness temperature of the core in K, which is presented in column 7 in Table 6 using the following equation:

$$T_b = 1.22 \times 10^{12} \frac{S}{\nu^2 d_{maj} d_{min}} (1 + z), \qquad (1)$$

where S is the flux density of the core and jet in Jy, z is the redshift, ν is the observing frequency in GHz, and d is the fitted Gaussian size (FWHM) of each component in mas.
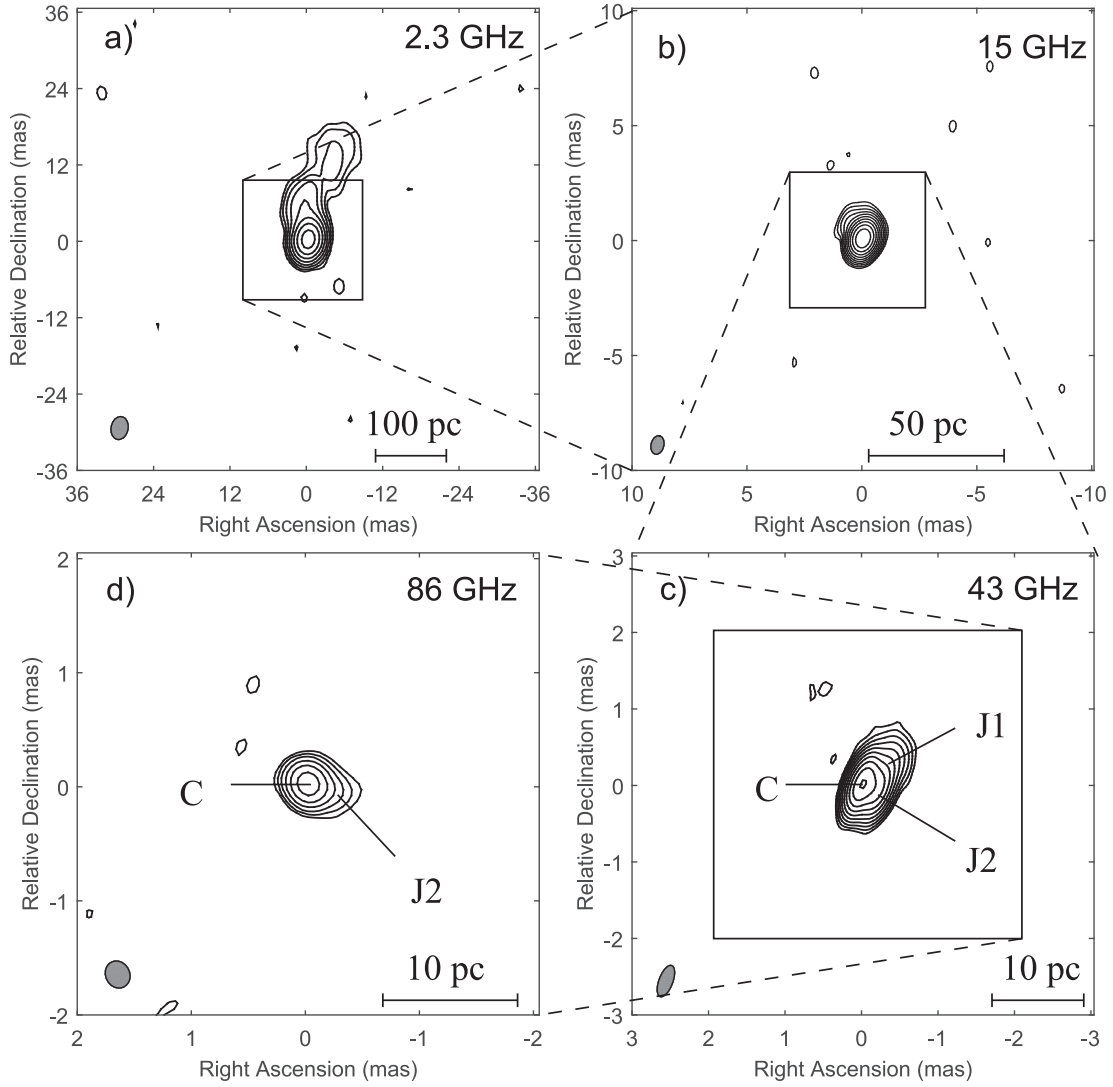
Figure 4. Naturally weighted total intensity VLBI images of 1030+415 at 2.3, 15, 43 GHz, and a uniformly weighted total intensity image at 86 GHz. The image parameters and references are given in Table 3.

Nine sources have T_b higher than 10^{11} K at 43 GHz, suggesting beamed jet emission. 2201+315 has a lower brightness temperature of 3.4×10^{10} K than others, but this relatively lower value is consistent with its classification as an FR II source. For every source, the 86 GHz T_b is lower than its 43 GHz value.

3.4. Comments on Individual Objects

Here, we report on the properties of each source with particular emphasis on jet morphology and kinematics obtained from previous studies and a comparison with our observations. Statistical studies of compactness, brightness temperatures, Doppler factors, and radio-γ-ray correlation based on a large sample containing 134 sources will be presented in a forthcoming paper (X.-P. Cheng et al. 2018, in preparation).

3.4.1. 0202+319 (J0205+3212)

The radio quasar J0205+3212 is at a redshift of $z = 1.466$ (Burbidge 1970). It was detected with the Large Area Telescope (LAT) on board the *Fermi* Gamma-ray Space Telescope (*Fermi*) in the 100 MeV–300 GeV energy range

(Abdo et al. 2010; Nolan et al. 2012; Acero et al. 2015). In the radio, the source shows a core and an extended component 15 arcsec to the north of the core in the 1.4 GHz Very Large Array (VLA) A-array configuration image. The flux densities of the core and the extended component are 652 mJy and 13 mJy, respectively (Cooper et al. 2007). The extended feature was not detected in the higher-resolution 8.4 GHz VLA image, and the core was detected with a flux density of 765 mJy (Healey et al. 2007).

On mas scales, the source is dominated by a compact core with a curved jet extending to the north and then to the northwest, as was seen previously at 1.4 GHz,[10] 5 GHz (Linford et al. 2012), 2.3 and 8.4 GHz (Beasley et al. 2002), and 15 GHz VLBA images (Lister et al. 2009). The intriguing feature of this source is the large jet bending from the north to the west with a position angle changing nearly 90° (Figures 2(a)–(b)). The jet first points to the north until 7 mas (a projected distance of ~55 pc north of the core), where it bends with a gradually changing position angle from 0° to

---

[10] Observed in the VLBA project BG196 (PI: D. Gabuzda), calibrated data downloaded from the Astrogeo database (http://astrogeo.org/).
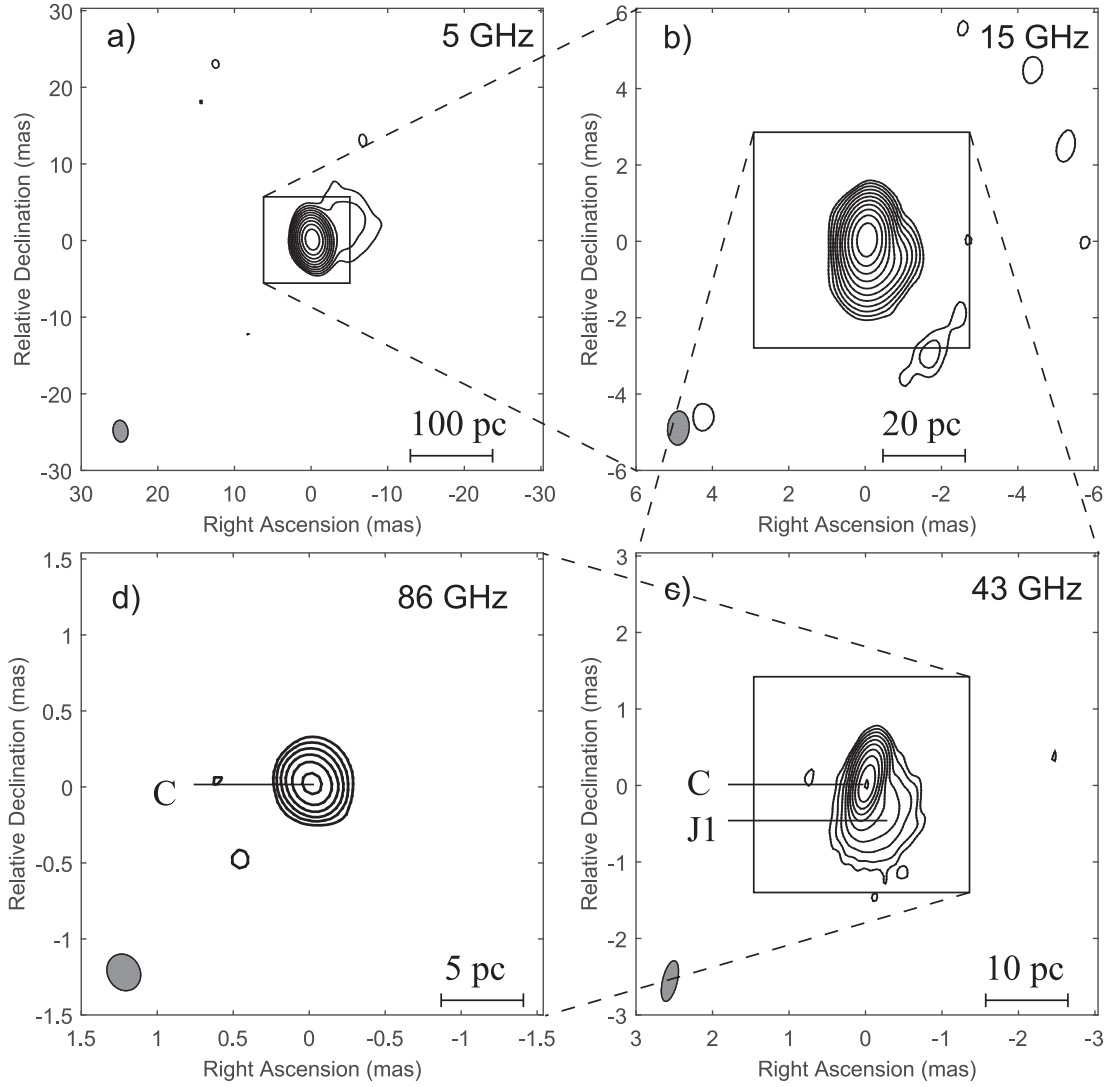
Figure 5. Naturally weighted total intensity VLBI images of 1128+385 at 5, 15, 43 GHz, and a uniformly weighted total intensity image at 86 GHz. The image parameters and references are given in Table 3.

$-64°$ at 35 mas (a projected distance of $\sim$280 pc away from the core).

Our 43 GHz image (Figure 2(c)) reveals the inner jet structure. Two new jet components, J1 and J2, are detected within 1 mas, at position angles of $-4°$ and $-55°$, respectively. The high-resolution 86 GHz image shows a core–jet morphology (Figure 2(d)). The 86 GHz observation was made only 9 days after the 43 GHz observation. We calculated the core spectral index $\alpha_{43-86} = -1.4$. It is much steeper than the spectral index $\alpha_{8.1-15.4}$ (Hovatta et al. 2014), indicating that the core (jet base) becomes optically thin at 86 GHz. The 86 GHz jet is at a slightly different position angle of 40° from that in the 43 GHz image and its position is between the two 43 GHz jet components. Due to the different frequencies and different (u, v) samplings at 43 and 86 GHz, accurate correspondence of the components is difficult. J1 is also detected in the innermost jet in the 15 GHz images at similar distance and position angles (Lister et al. 2009). In combination with the lower-frequency VLBI images, the parsec-scale jet exhibits a wiggling track: the jet direction starts at a position angle of $\sim$$-55°$ (J2) then bends to P.A. $\sim$ $-4°$ at J1; the position angle gradually changes from 0° at $\sim$7 mas to $-64°$ until 35 mas. This might result from a

projection on the plane of the sky of a helically twisted jet. Helical jets could be triggered by periodic variation in the direction of jet ejection (Linfield 1981; Stirling et al. 2003; Zhao et al. 2011), Kelvin–Helmboltz instabilities in the jet flow (Hardee 2003; Feng et al. 2005; An et al. 2010), or the magnetohydrodynamics of the jet (Camenzind 1986), and can result in quasi-periodic flux density variability (Camenzind & Krockenberger 1992; An et al. 2013; Wang et al. 2014; Mohan & Mangalam 2015). The 15 GHz VLBA monitoring observation inferred superluminal motions of two jet components from 14-epoch data sets between 1995 and 2010, with a proper motion of 148 ± 15 μas yr^{-1} (10.1 c) at about 7 mas and 36 ± 13 μas yr^{-1} (2.47 c) at about 1.5 mas from the core (Lister et al. 2013). As the jet kinematics indicate apparent superluminal knot speeds, which result in a very small viewing angle, it could also be the case that small intrinsic jet bends are exaggerated by projection and Doppler-beaming effects.

3.4.2. 0529+483 (J0533+4822)

This is a quasar at a redshift of $z = 1.16$ (Shaw et al. 2012). *Fermi*/LAT detected the source in the 100 MeV to 300 GeV
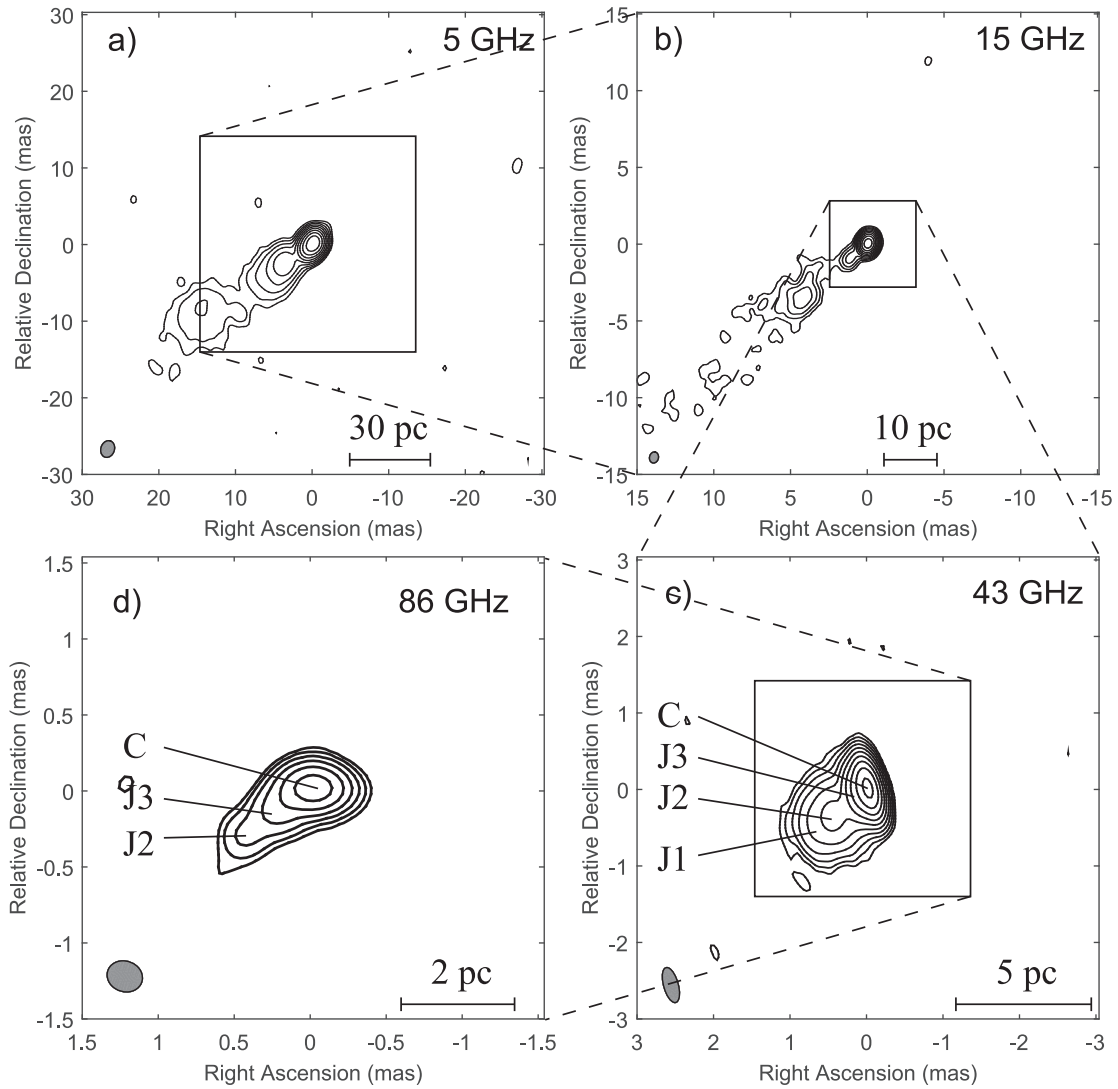
Figure 6. Naturally weighted total intensity VLBI images of 1418+546 at 5, 15, 43 GHz, and a uniformly weighted total intensity image at 86 GHz. The image parameters and references are given in Table 3.

energy band with a significance of 32.9σ in the third *Fermi* source catalog (3FGL; Acero et al. 2015). The source 0529 +483 has a complex radio spectrum: a steep spectrum with a spectral index of $\alpha = -0.95$ between 74 MHz and 350 MHz (NED[11]), a slightly inverted spectrum with $\alpha = 0.04$ between 8.1 and 15.4 GHz (Hovatta et al. 2014), and a flat spectrum with $\alpha = -0.1$ shown in the *WMAP* data between 33 and 94 GHz (Gold et al. 2011). The 1.4 GHz VLA image shows a core and a northeastern lobe (Cooper et al. 2007). There is diffuse structure to the southwest of the core in the opposite direction of the northeast lobe. The kiloparsec-scale structure can be described as a triple structure with a core and double lobes. The core flux density from a 5 GHz high-resolution VLA observation is 818 mJy (Laurent-Muehleisen et al. 1997). There is a difference of 229 mJy between the total flux densities measured by the VLA and the 300-foot Green Bank Telescope at 5 GHz (Gregory et al. 1996), suggesting the existence of extended structure is consistent with its steep low-frequency spectrum below 350 MHz.

The VLBA images show a core and a one-sided jet structure extending to the northeast out to ~ 30 mas (Figure 3(a)), roughly in alignment with the kiloparsec-scale jet direction (Beasley et al. 2002; Lister et al. 2016). The 15 GHz image shown in Figure 3(b) shows a core and a northeast jet to a distance of 4 mas. The long-term VLBA monitoring observations at 15 GHz from 2002 to 2013 detected superluminal motions of 4 jet components with a maximum speed of 19.8 c (Lister et al. 2016).

We present for the first time the 43 and 86 GHz total intensity images of this source. The 43 GHz image in Figure 3(c) shows a new jet J1 component appearing ~ 0.45 mas to the northeast of the core. The jet direction is consistent with that shown in the 15 GHz image. The 86 GHz image only detected a compact naked core. J1 is resolved at 86 GHz. The VLBA and VLA images indicate that the jet follows a straight trajectory from parsec to kiloparsec scales without significant jet bending. The two-frequency observations have a time separation of 9 days. We calculated the core spectral index $\alpha_{43-86} = -0.3$. It suggests a flat spectrum, but is still steeper than the spectral index $\alpha_{8.1-15.4}$ derived from the *WMAP* data (Gold et al. 2011).

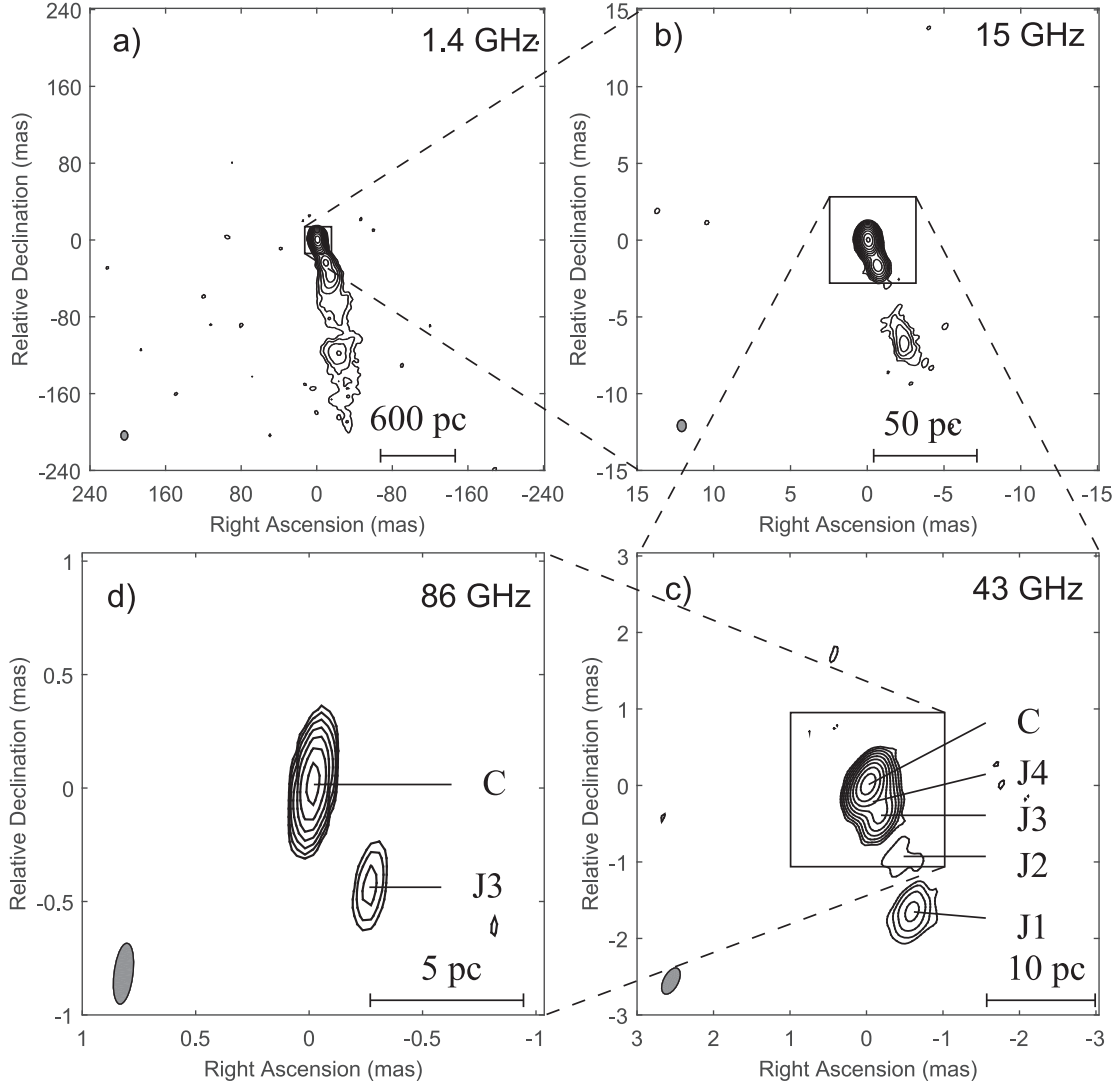
[11] http://ned.ipac.caltech.edu/

Figure 7. Naturally weighted total intensity VLBI images of 1823+568 at 1.4, 15, 43 GHz, and a uniformly weighted total intensity image at 86 GHz. The image parameters and references are given in Table 3.

3.4.3. 1030+415 (J1033+4116)

The radio quasar 1030+415 is at a redshift of $z = 1.1185$ (Hewett & Wild 2010) and significant γ-ray emission of 24.7σ was detected by *Fermi*/LAT (Acero et al. 2015). The VLA in its A-array configuration at 1.4 GHz detected a one-sided jet extending to the east to about 0.5 arcsec (Xu et al. 1995). This jet was marginally detected in the Faint Images of the Radio Sky at Twenty-Centimeters survey with the VLA B-array at 1.4 GHz (White et al. 1997). At 8.4 GHz the VLA observation revealed a point source with a flux density of 384.4 mJy (Healey et al. 2007).

VLBA images at 5 GHz (Helmboldt et al. 2007), 1.7 GHz (Polatidis et al. 1995), 2.3 (Figure 4(a)), and 8.4 GHz (Fey et al. 2004) display a jet extending to the north at a distance of about 10 mas, then bending to the northwest out to about 15 mas. The 15 GHz MOJAVE images (Figure 4(b)) of the source detected a naked core in six epochs during 2010 September and 2013 July, and only showed a marginal hint of a weak northeastern jet in the latest epoch (Lister et al. 2016).

Figures 4(c)–(d) present the 43 and 86 GHz images of 1030 +415 with a high resolution of ∼0.18 mas (corresponding to

1.5 pc). The core that was unresolved in 15 GHz images is resolved into a core and inner jet structure. Two new jet components are detected within 0.5 mas in the 43 GHz image: J2 at 0.19 mas away from the core in a position angle of $-110°$, and J1 at 0.41 mas in P.A. $= -54°$. J2 is also detected at 86 GHz at 0.14 mas, in P.A. $= -105°$. The overall jet morphology shows an oscillatory trajectory with multiple bends within 20 mas: bending from southwest to northwest at ∼0.2 mas; and from northwest to north (and slightly northeastern) until 10 mas, where the jet bends to northwest until ∼20 mas. One possibility is that this source contains a helical jet. Further discussion of the physical driving mechanisms of helical jets is presented in Section 3.4.1. We found that the source is not substantially variable at 15 GHz (Richards et al. 2011). The flux densities at 15 GHz between the two epochs differ by less than 10%.

3.4.4. 1128+385 (J1130+3815)

1128+385 (B2 1128+38) is a low-spectral peaked source at a redshift of $z = 1.733$ (Schneider et al. 2007) and an optically violent quasar (Véron-Cetty & Véron 2010). It was not
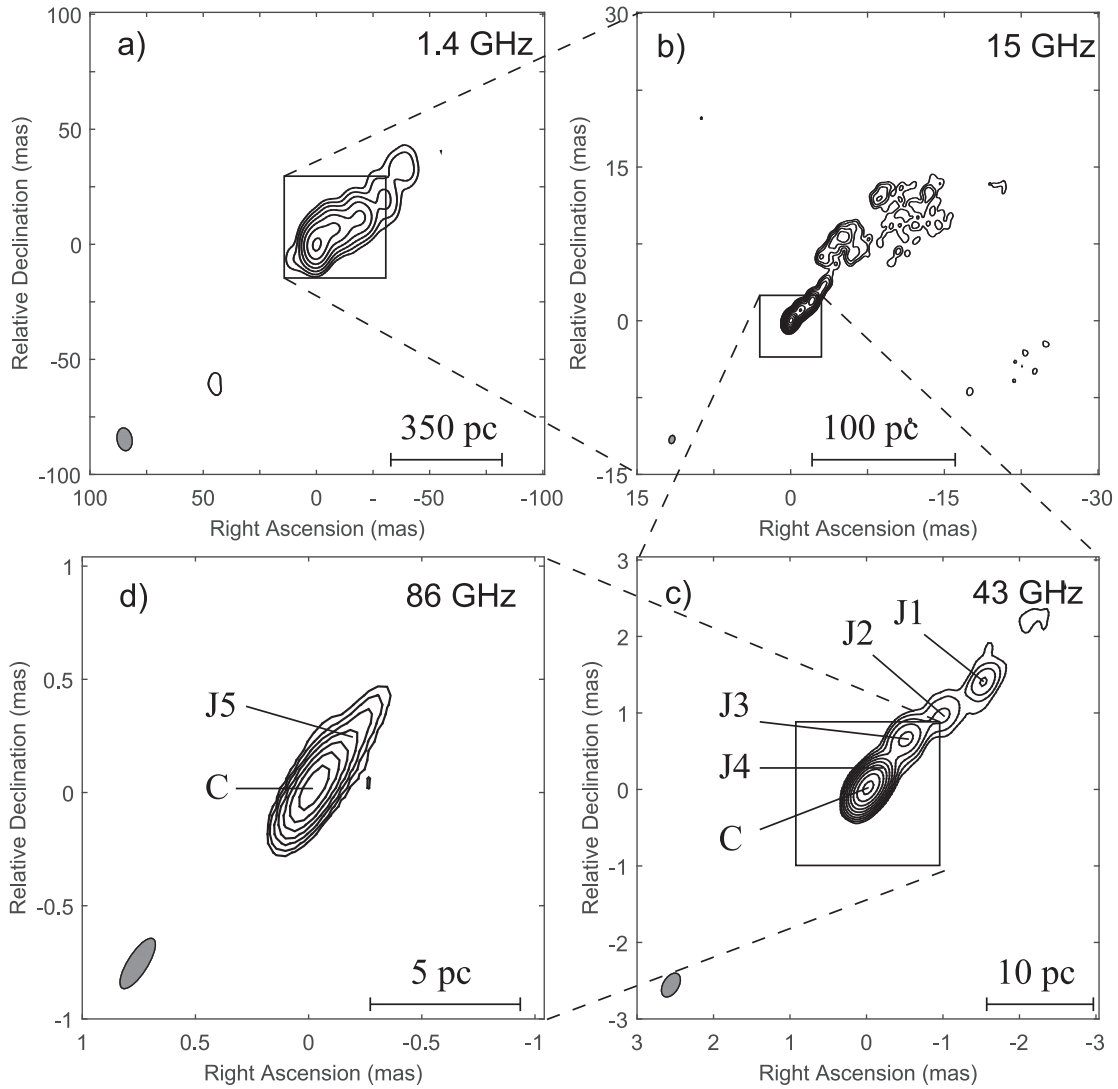
Figure 8. Naturally weighted total intensity VLBI images of 1828+487 at 1.4, 15, 43 GHz, and a uniformly weighted total intensity image at 86 GHz. The image parameters and references are given in Table 3.

detected by the Energetic Gamma Ray Experiment Telescope (EGRET) on board the *Compton Gamma Ray Observatory* satellite, but was detected by *Fermi*/LAT at a level of 5.5σ (Acero et al. 2015). The 1.6 GHz VLA image in the combined A+B-array configuration shows a compact core and a hint of a weak feature at $15''$ ($\sim$130 kpc) southeast of the core (Murphy et al. 1993).

The snapshot VLBI images derived from the VLBI calibrator survey[12] only show a naked core at 2.3 and 8.4 GHz. In a 5 GHz VLBI observation (Figure 5(a)), Xu et al. (1995) detected a weak extended jet to the west of the compact core. The higher-resolution 15 GHz VLBA images (Figure 5(b)) show that the jet points toward the southwest to a distance of 1.5 mas (corresponding to a projected distance $\sim$12.8 pc). The maximum jet speed is $3.29 \pm 0.28\,c$ (Lister et al. 2016).

The 43 GHz image derived from our observations is shown in Figure 5(c) and resolves the source into a core and a southwestern jet component J1. The jet shows an extension to the west from J1, in good agreement with the outer jet that is

seen in the 15 GHz image (Lister et al. 2016). The 86 GHz image from Lee et al. (2008) shows a core and a weak jet ($\sim$6σ) to the southwest at 0.21 mas. However, our new 86 GHz VLBA image in Figure 5(d) only shows a compact core with a flux density of 170 mJy, although it has a much higher sensitivity compared to the previous image. We note that the total flux densities between the two 86 GHz data sets differ by 370 mJy; the non-detection of the jet component at about 0.2 mas is probably due to variability. The southwestern jet J1 seen in the 43 GHz image was resolved in our 86 GHz image.

3.4.5. 1418+546 (J1419+5423)

1418+546 (OQ 530) is a BL Lac source at a redshift of $z = 0.153$ (Shaw et al. 2012). It was not detected by the EGRET, but detected by *Fermi*/LAT (3FGL J1419.9+5425) with 20.1σ (Acero et al. 2015). The 1.6 GHz VLA map displays a one-sided kiloparsec-scale halo with a component west of the compact core at a separation of about $32''$ (Murphy et al. 1993). The diffuse halo was also detected in the 1.4 GHz VLA D-array image (Cassaro et al. 1999). The western lobe was confirmed by the 1.4 GHz observations made by the VLA

---

[12] The VLBA calibrator survey database is maintained by Leonid Petrov at http://astrogeo.org/.
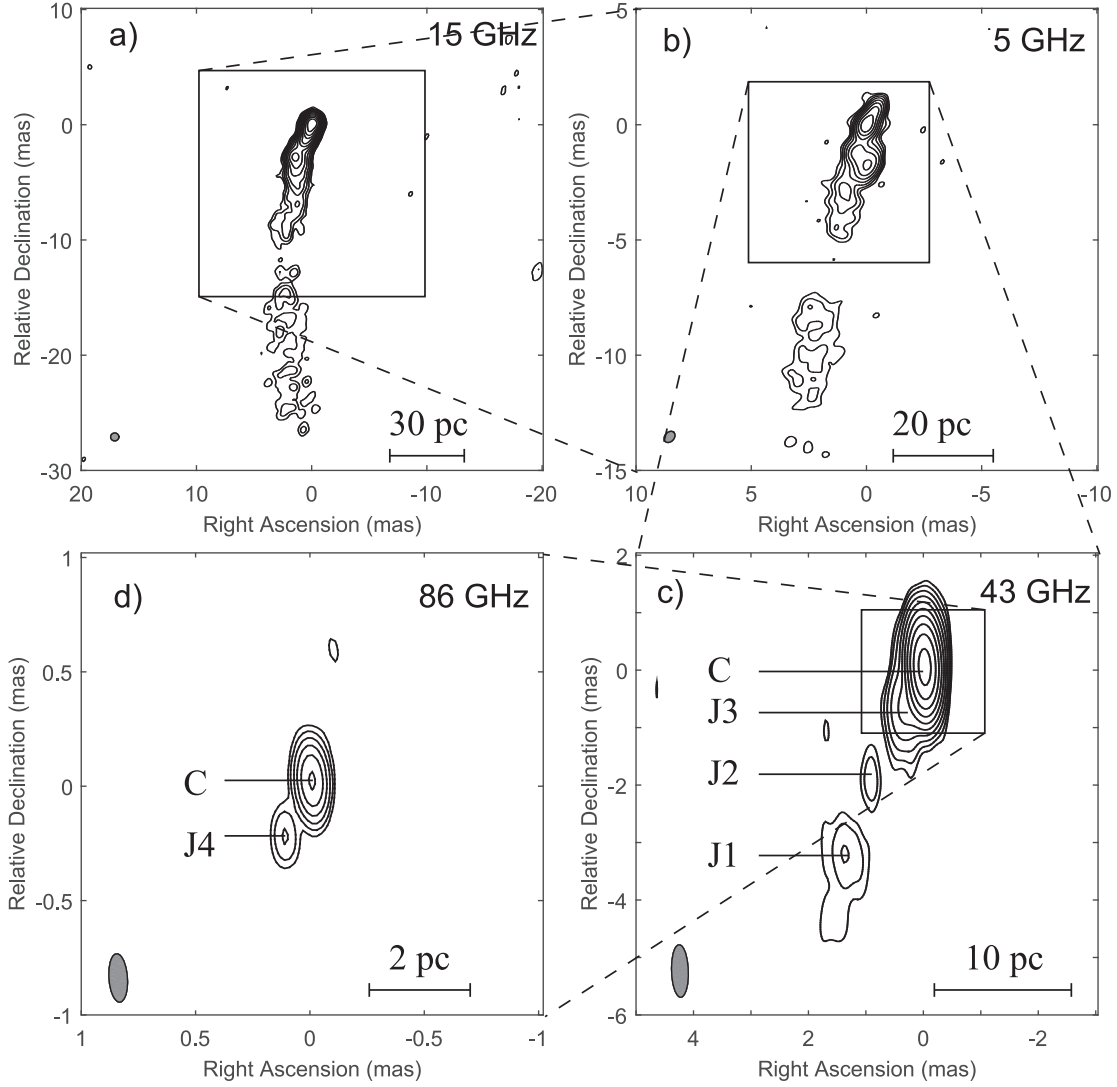
Figure 9. Naturally weighted total intensity VLBI images of 1928+738 at 15, 5, 43 GHz, and a uniformly weighted total intensity image at 86 GHz. The 5 GHz image is from the VSOP observation, and the angular resolution is better than that of a MOJAVE image. The image parameters and references are given in Table 3.

in its B-array configuration and the Westerbork Synthesis Radio Telescope (Cassaro et al. 1999). However, the VLBI images revealed a single-sided jet to the southeast, in an opposite direction of the kiloparsec-scale lobe: the 5 GHz VLBA image (Figure 6(a)) shows the jet extending to the southeast to approximately 25 mas (Helmboldt et al. 2007); the 15 GHz VLBA image (Figure 6(b), Lister et al. 2016) shows a consistent morphology with the 5 GHz image. The VLBA structure does not show rapid structural change or superluminal motion. A maximum jet speed of $0.93 \pm 0.27\,c$ was determined based on the 15 GHz data over a time baseline of 18 years from 1995 to 2013 (Lister et al. 2016).

We present the first 43 and new 86 GHz VLBA images (Figures 6(c)–(d)) of this source. The direction of the inner 1 mas jet is in excellent agreement with that derived from the 5 and 15 GHz images (Figures 6(a)–(b)). The innermost jet component J3 is at ~0.2 mas at a P.A. of ~120°, corresponding to a projected linear size of 0.5 pc. Two outer jet components, J1 and J2, were also detected at 15 GHz. The jet components J2 and J3 are also detected in the 86 GHz image. The brightness temperature of the core is 3.8×10^{10} K at 86 GHz, showing no evidence of strong Doppler boosting, consistent with the slow

jet motion. The OVRO 40 m 15 GHz light curve shows that the flux density does not undergo significant variation from 2008 to mid-2013 (Richards et al. 2011). After experiencing a long "quiet" period, the source flared in early 2014. An even larger flare started in 2015 and peaked at the beginning of 2016. Our observations were carried out before the 2016 flare. Due to its high flux density and compact structure, 1418+546 can be used as a flux density scale calibrator for mm and sub-mm VLBI observations, e.g., the EHT and Atacama Large Millimeter/ submillimeter Array observations.

3.4.6. 1823+568 (J1824+5651)

1823+568 (4C +56.27) is a BL Lac object at a redshift $z = 0.664$ (Lawrence et al. 1986), but Véron-Cetty & Véron (2006) classified this source as a quasar. The source was listed in the *Fermi*/LAT AGN catalog as 3FGL J1824.2+5649 and was detected at a significance level of 34.5 σ (Acero et al. 2015). The VLA images at 1.6 GHz (Murphy et al. 1993) and 5 GHz (Kollgaard et al. 1992) show a prominent core–jet morphology with the jet extending toward the east up to ~5″. A diffuse halo surrounds the compact core–jet structure. The
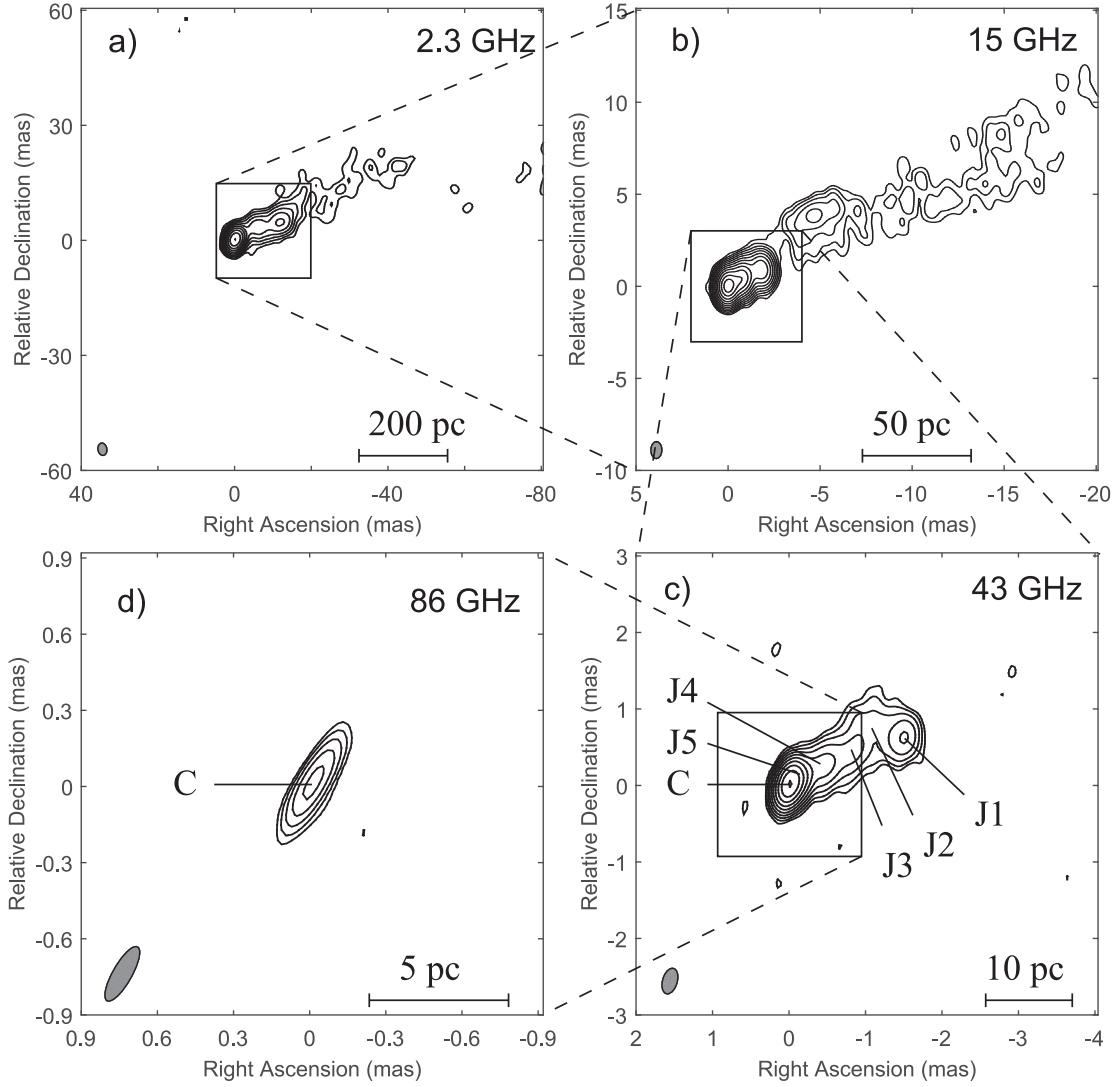
Figure 10. Naturally weighted total intensity VLBI images of 1954+513 at 2.3, 15, 43 GHz, and a uniformly weighted total intensity image at 86 GHz. The image parameters and references are given in Table 3.

radio spectrum is flat above 1 GHz, but steep below 1 GHz, indicative of an extended steep-spectrum halo.

The low-frequency VLBA images (Figures 7(a)–(b)), however, show a jet extending to the south to a maximum distance of ∼200 mas (Pearson & Readhead 1988; Gabuzda & Cawthorne 1996; Lister et al. 2016). The total flux density at 15 GHz shows moderate-level variability (Richards et al. 2011). The ratio of $(S_{max} - S_{min})/(S_{max} + S_{min})$ is only 0.18.

Our high-sensitivity 43 and 86 GHz images (Figures 7(c)–(d)) reveal rich jet structures on scales of 2 mas (14 pc) and 0.5 mas (3.5 pc), respectively. Four jet components are identified at 43 GHz, and they were also detected at 15 GHz (Lister et al. 2016). These jet components show complex motions, with a mixture of superluminally moving (J1 and J2) and stationary jet knots (J3 and J4). The maximum proper motion 576 ± 48 μas yr^{-1} $(21.9 \pm 1.8c)$ is associated with a jet component at 6.3 mas from the core (Lister et al. 2016). Compared with the 15 GHz image, the 43 GHz image shows a pronounced emission gap between 1.1 mas and 1.8 mas. The jet in 1823 +568 likely consists of both fast-moving knots that were detected at all frequencies, and a slowly moving underlying flow that is resolved out in the 43 GHz image. The 86 GHz image obtained by Lee et al. (2008) shows a naked core with a flux density of 485 mJy. The core flux density from our 86 GHz data is 230 mJy, much smaller than that obtained by Lee et al. (2008), indicating variability between the two epochs.

3.4.7. 1828+487 (J1829+4844)

The radio source 1828+487 (3C 380) is at a redshift of $z = 0.692$ (Lawrence et al. 1996). The *Fermi*/LAT identified the source as 3FGL J1829.6+4844 with a 24.1σ detection significance in the 100 MeV–300 GeV energy range (Acero et al. 2015). The image made with the VLA in A+B-array at 1.6 GHz shows a large diffuse halo with a size of 6″ surrounding a central compact component (Murphy et al. 1993). The source was mapped with the Multi-Element Radio Linked Interferometer Network, which detected structure up to an overall angular extent of about 6″ (corresponding to a linear size of ∼50 kpc). The radio morphology suggests that the source belongs to the class of compact steep-spectrum (CSS) sources (Wilkinson et al. 1984; Fanti et al. 1985).
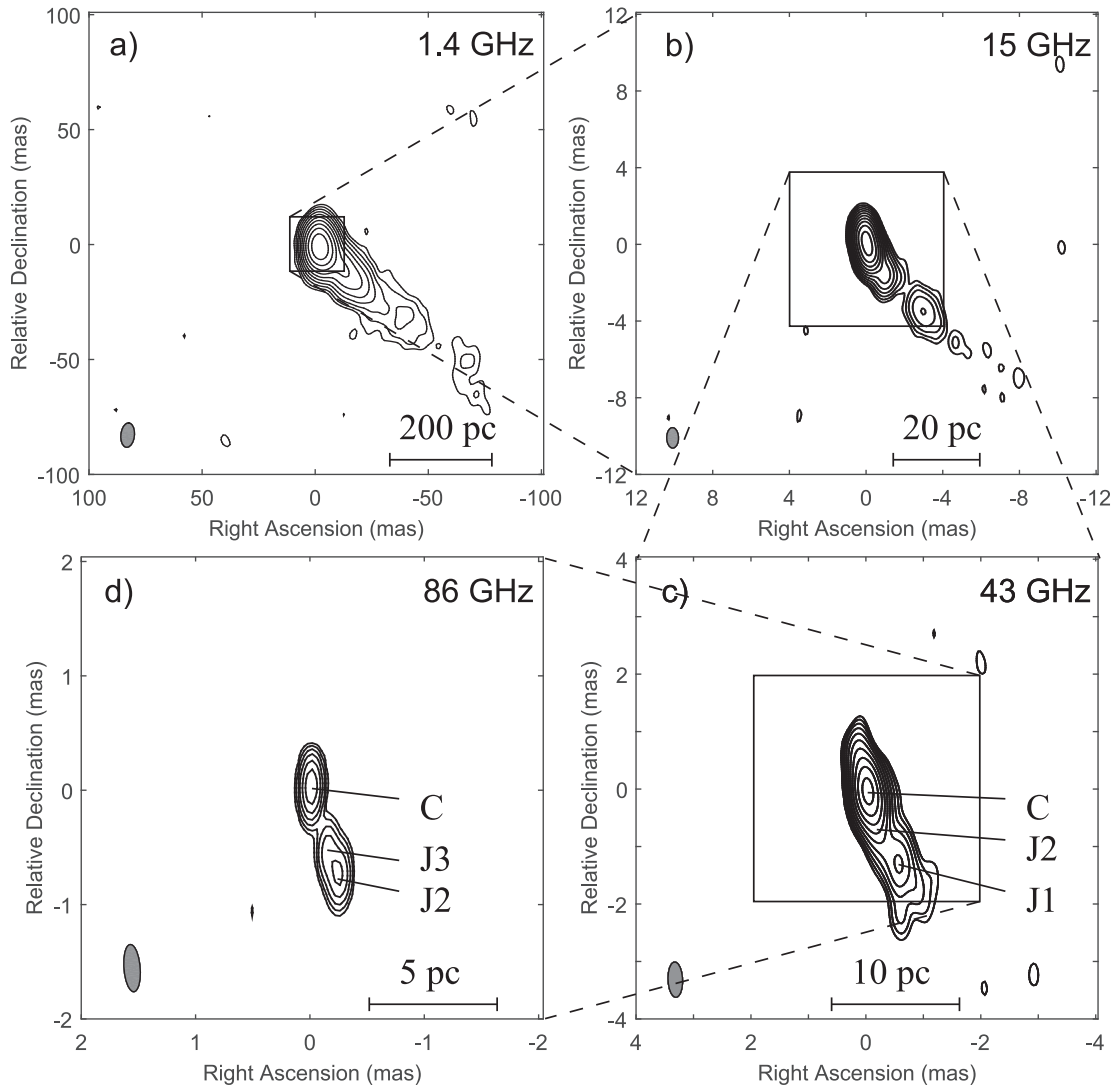
Figure 11. Naturally weighted total intensity VLBI images of 2201+315 at 1.4, 15, 43 GHz, and a uniformly weighted total intensity image at 86 GHz. The image parameters and references are given in Table 3.

In the 1.4 GHz VLBI image (Figure 8(a)), the jet extends to the northwest out to a distance of 70 mas. The jet body is characterized by a chain of bright knots, similar to another archetypal CSS quasar, 3C 48 (Wilkinson et al. 1991). The 5 GHz VLBA data revealed an isolated bright knot at 732 mas (≥ 20 kpc de-projected) downstream of the jet at a position angle around $-52°$, in good alignment with the inner parsec-scale jet (Koyama et al. 2013). The VLBI Space Observatory Programme (VSOP) 5 GHz image revealed a fine structure along the parsec-scale jet, which is in good agreement with the low angular resolution image (Lister et al. 2001). The 15 GHz images (Figure 8(b)) obtained from the MOJAVE data show that the inner 3 mas jet points to a position angle of $-70°$, slightly different from the outer jet. From about 10 mas, a plume-like diffuse emission appears to the west of the jet body. Proper motions were determined for eight jet components from the MOJAVE program, with the maximum proper motion of 0.33 mas yr^{-1} (13.06 ± 0.14 c) (Lister et al. 2013).

Our 43 GHz image (Figure 8(c)) displays rich jet structure to a distance of about 3 mas, and four bright knots are identified. J1 and J2 roughly correspond to components No. 8 and 10 in Lister et al. (2016). But cross-matching of J3 and J4 with their counterparts in the 15 GHz images is difficult due to the different resolutions. The early 86 GHz image detected a compact core and a secondary component (5σ) at about 4 mas to the northwest in a position angle $-31°$ (Lee et al. 2008). This 4 mas jet component is not detected in our 43 and 86 GHz images. Our new 86 GHz image (Figure 8(d)), having a higher sensitivity than previous observations at this frequency, reveals the inner core–jet structure within 0.7 mas. A jet component J5 was identified, but it does not exactly correspond to J4. Comparing the high-frequency images with sub-mas resolution with those at lower resolutions shows a change of the position angles with the distance from the core, suggesting a possible wiggling trajectory. However, the study of Lister et al. (2013) finds that the jet shows moving features along independent trajectories with different vector motion position angles, indicating that the ejection of the knots is occurring at different position angles.

3.4.8. 1928+738 (J1927+7358)

1928+738 (4C +73.18) is a low-spectral peaked AGN at a redshift of $z = 0.302$ (Lawrence et al. 1996). The source was

Table 3
Image Parameters

IAU Name (1)	Epoch (yyyy mm dd) (2)	ν (GHz) (3)	S_{tot} (Jy) (4)	S_{peak} (Jy beam^{-1}) (5)	B_{maj} (mas) (6)	B_{min} (mas) (7)	θ (°) (8)	σ (mJy beam^{-1}) (9)	Figure (10)	References (11)
0202+319	2010 Mar 07	1.4	0.78	0.54	10.18	6.43	−2.98	0.16	2a	2
	2005 Sep 05	15	1.85	1.73	0.98	0.60	−15.1	0.25	2b	3
	2014 Nov 21	43	1.04	0.79	0.52	0.24	−22.30	0.29	2c	1
	2014 Nov 30	86	0.32	0.26	0.35	0.18	46.50	2.10	2d	1
0529+483	2010 Jun 18	1.4	0.50	0.39	9.08	7.08	1.15	0.13	3a	2
	2013 Mar 31	15	2.10	1.99	0.84	0.71	−16.60	0.70	3b	5
	2014 Nov 21	43	0.35	0.30	0.51	0.31	5.75	0.30	3c	1
	2014 Nov 30	86	0.26	0.24	0.34	0.18	79.30	1.83	3d	1
1030+415	2000 Jul 06	2.3	0.31	0.23	3.60	2.64	−11.34	0.40	4a	4
	2013 Jul 30	15	1.19	1.02	0.81	0.55	−13.60	0.80	4b	5
	2015 Mar 08	43	0.68	0.44	0.43	0.18	−20.50	0.28	4c	1
	2014 Nov 29	86	0.22	0.19	0.24	0.20	26.10	1.33	4d	1
1128+385	1996 Aug 22	5	1.00	0.93	2.82	1.92	7.07	0.30	5a	6
	2013 Feb 10	15	1.33	1.10	0.88	0.56	−4.60	0.50	5b	5
	2015 Mar 08	43	0.72	0.53	0.54	0.19	−13.20	0.29	5c	1
	2014 Nov 29	86	0.18	0.17	0.25	0.21	29.60	1.37	5d	1
1418+546	1996 Aug 17	5	0.66	0.43	2.21	1.76	−18.71	0.20	6a	7
	2013 Jun 02	15	0.60	0.50	0.72	0.58	−12.90	0.60	6b	5
	2015 Mar 08	43	1.30	0.83	0.47	0.19	15.70	0.36	6c	1
	2014 Nov 29	86	0.31	0.19	0.23	0.20	71.2	1.20	6d	1
1823+568	2010 Jul 29	1.4	0.76	0.50	8.94	6.93	1.69	0.10	7a	2
	2012 Mar 27	15	1.54	1.22	0.75	0.57	0.30	0.50	7b	5
	2015 Jan 10	43	0.65	0.46	0.37	0.19	−27.60	0.25	7c	1
	2016 May 06	86	0.24	0.22	0.24	0.07	−7.04	1.07	7d	1
1828+487	2010 Aug 23	1.4	2.51	0.88	9.93	6.57	10.58	3.30	8a	2
	2016 Nov 18	15	1.82	1.21	0.80	0.55	−15.70	0.50	8b	10
	2015 Jan 10	43	1.13	0.89	0.34	0.20	−31.20	0.32	8c	1
	2016 May 06	86	0.27	0.22	0.25	0.08	−32.30	0.75	8d	1
1928+738	2013 Jan 21	15	3.38	1.93	0.71	0.68	−86.90	0.18	9a	5
	1997 Aug 22	5	3.32	0.92	0.54	0.40	−42.00	0.30	9b	8
	2015 Jan 10	43	3.88	3.31	0.91	0.29	1.87	1.00	9c	1
	2016 May 06	86	0.23	0.20	0.21	0.08	3.96	1.90	9d	1
1954+513	1999 Mar 08	2.3	1.09	0.65	3.21	2.30	8.80	0.30	10a	9
	2016 Nov 12	15	1.13	0.65	0.91	0.58	−0.80	0.24	10b	10
	2015 Jan 10	43	0.71	0.50	0.34	0.19	−16.00	0.30	10c	1
	2016 May 06	86	0.17	0.18	0.24	0.07	−29.60	2.90	10d	1
2201+315	2007 Apr 30	1.4	1.53	1.05	10.55	5.94	−5.94	0.30	11a	2
	2017 Jan 28	15	2.50	1.53	1.06	0.61	1.00	1.00	11b	10
	2015 Jan 10	43	1.21	0.80	0.61	0.25	2.23	0.40	11c	1
	2016 May 06	86	0.53	0.30	0.34	0.10	1.21	1.83	11d	1

Note. (1) Source name (B1950.0); (2) observing epoch; (3) frequency; (4) integrated flux density; (5) peak specific intensity; (6) major axis of the restoring beam (FWHM); (7) minor axis of the restoring beam (FWHM); (8) position angle of the major axis, measured from north through east; (9) off-source rms noise in the clean image; (10) the corresponding figure number of the image (11). References for the images: (1) this paper, (2) http://astrogeo.org/, (3) Lister et al. (2009), (4) Fey et al. (2004), (5) Lister et al. (2016), (6) Xu et al. (1995), (7) Helmboldt et al. (2007), (8) Lister et al. (2001), (9) Pushkarev & Kovalev (2012), (10) MOJAVE database http://www.physics.purdue.edu/astro/MOJAVE/allsources.html.

not detected by EGRET or *Fermi*/LAT. The VLA image shows a core with jets and diffuse emission. A series of at least four bright components extends 18″ to the south and the jet gradually bends from the south to the southeast (Murphy et al. 1993). To the north of the core, there is one bright hotspot about 1″ from the core and a large patch of diffuse emission beyond the hotspot (Rusk & Rusk 1986; Johnston et al. 1987; Kollgaard et al. 1990).

Lister et al. (2001) presented a 5 GHz VSOP image (Figure 9(b)) showing 5 jet components within 6 mas that seem to indicate a helical trajectory. The kinematics of the jet at 15 GHz (Figure 9(a)) and 43 GHz (Lister 2001) provided a means of constraining the black hole spin (Kun et al. 2014).

The maximum jet speed is $8.16 \pm 0.21c$ among 13 moving features (Lister et al. 2013).

We present our new 43 GHz image (Figure 9(c)), showing the inner 3 mas jet. The 43 GHz image shows 3 jet components, at varying position angles, consistent with the suggested helical jet structure inferred from the 5–15 GHz VLBI images. A published snapshot 86 GHz VLBI image only detected the core feature (Lee et al. 2008). Our new 86 GHz data (Figure 9(c)–(d)) revealed a new jet component J4 at a distance of 0.31 mas and P.A. of 160°. The 86 GHz flux density of the core is less than 10% of that at 43 GHz, probably the result of the observation at 43 GHz during or just after the flare and the 86 GHz observation during the declining phase or near

Table 4
Model-fitting Parameters

IAU Name (1)	ν (GHz) (2)	Comp. (3)	S_{tot} (mJy) (4)	S_{peak} (mJy beam^{-1}) (5)	R (μas) (6)	P.A. (°) (7)	d_{maj} (μas) (8)	d_{min} (μas) (9)
0202+319	43	C	804 ± 40	790 ± 40	...	...	126 ± 19	75 ± 19
		J2	164 ± 8	440 ± 22	180 ± 34	−56.3	228 ± 34	...
		J1	36 ± 2	150 ± 8	477 ± 70	−4.2	464 ± 70	...
	86	C	290 ± 29	260 ± 26	...	...	80 ± 12	80 ± 12
		J2	26 ± 3	24 ± 2	289 ± 44	−14.9	290 ± 44	...
0529+483	43	C	320 ± 16	300 ± 15	...	...	100 ± 15	100 ± 15
		J1	31 ± 2	43 ± 2	454 ± 113	26.9	759 ± 113	...
	86	C	260 ± 3	240 ± 2	...	...	80 ± 12	80 ± 12
1030+415	43	C	460 ± 23	440 ± 22	...	...	110 ± 17	40 ± 17
		J2	180 ± 9	200 ± 10	190 ± 17	−110.7	110 ± 17	...
		J1	40 ± 2	57 ± 3	410 ± 36	−54.1	240 ± 36	...
	86	C	200 ± 20	190 ± 19	...	...	60 ± 9	60 ± 9
		J2	60 ± 6	26 ± 3	140 ± 15	−104.5	100 ± 15	...
1128+385	43	C	510 ± 26	530 ± 27	...	...	50 ± 8	50 ± 8
		J1	200 ± 10	21 ± 1	210 ± 20	−10.5	130 ± 20	...
	86	C	170 ± 17	170 ± 17	...	...	30 ± 5	30 ± 5
1418+546	43	C	860 ± 43	830 ± 42	...	...	80 ± 12	70 ± 11
		J3	210 ± 11	260 ± 13	170 ± 18	115.9	120 ± 18	...
		J2	150 ± 8	54 ± 3	540 ± 63	129.4	420 ± 63	...
		J1	60 ± 3	26 ± 2	860 ± 60	127.9	400 ± 60	...
	86	C	240 ± 12	190 ± 10	...	...	200 ± 30	60 ± 30
		J3	50 ± 3	57 ± 3	270 ± 21	122.8	140 ± 21	...
		J2	20 ± 1	21 ± 1	560 ± 8	123.9	160 ± 8	...
1823+568	43	C	450 ± 23	450 ± 23	...	...	70 ± 11	40 ± 11
		J4	110 ± 6	190 ± 10	140 ± 26	−145.4	170 ± 26	...
		J3	60 ± 3	52 ± 3	450 ± 17	−157.9	110 ± 17	...
		J2	7 ± 1	2 ± 1	1070 ± 63	−155.2	420 ± 63	...
		J1	20 ± 1	12 ± 1	1820 ± 35	−161.0	230 ± 35	...
	86	C	230 ± 23	220 ± 22	...	...	50 ± 7	50 ± 7
		J3	20 ± 2	14 ± 1	490 ± 5	−151.2	30 ± 5	...
1828+487	43	C	886 ± 44	896 ± 45	...	...	90 ± 14	60 ± 14
		J4	159 ± 8	470 ± 24	137 ± 17	−43.6	110 ± 17	...
		J3	50 ± 3	70 ± 4	844 ± 33	−37.8	220 ± 33	...
		J2	20 ± 1	12 ± 1	1432 ± 57	−45.4	380 ± 57	...
		J1	17 ± 1	20 ± 1	2195 ± 21	−47.4	140 ± 21	...
	86	C	220 ± 22	221 ± 22	...	...	20 ± 3	20 ± 3
		J5	50 ± 5	94 ± 9	170 ± 15	−42.7	100 ± 15	...
1928+738	43	C	3750 ± 188	3388 ± 169	...	...	170 ± 26	80 ± 26
		J3	140 ± 7	135 ± 7	820 ± 47	153.9	310 ± 47	...
		J2	20 ± 1	16 ± 1	2220 ± 6	154.2	40 ± 6	...
		J1	40 ± 2	20 ± 1	3640 ± 68	157.2	450 ± 68	...
	86	C	210 ± 21	202 ± 20	...	...	40 ± 6	20 ± 6
		J4	30 ± 3	12 ± 1	310 ± 18	163.3	120 ± 18	...
1954+513	43	C	520 ± 26	497 ± 25	...	...	80 ± 12	50 ± 12
		J5	60 ± 3	26 ± 1	160 ± 14	−72.2	90 ± 14	...
		J4	50 ± 3	24 ± 1	510 ± 39	−61.2	260 ± 39	...
		J3	20 ± 1	11 ± 1	920 ± 42	−62.9	280 ± 42	...
		J2	30 ± 2	16 ± 1	1340 ± 81	−55.6	540 ± 81	...
		J1	30 ± 2	16 ± 1	1630 ± 33	−68.1	220 ± 33	...
	86	C	170 ± 17	180 ± 18	...	...	80 ± 12	80 ± 12
2201+315	43	C	1060 ± 53	797 ± 40	...	...	370 ± 56	90 ± 56
		J2	500 ± 25	408 ± 20	880 ± 24	−166.2	160 ± 24	...
		J1	70 ± 4	42 ± 2	1380 ± 35	−155.6	230 ± 35	...
	86	C	319 ± 32	303 ± 30	...	...	40 ± 6	40 ± 6
		J3	81 ± 8	62 ± 6	575 ± 6	−145.5	43 ± 6	...
		J2	132 ± 13	126 ± 13	821 ± 10	−162.5	66 ± 10	...

Note. (1) Source name (B1950.0); (2) observing frequency; (3) component name (4) model flux density; (5) peak specific density; (6) separation from the core; (7) position angle with respect to the core, measured from north through east; (8) major axis (FWHM); (9) minor axis (FWHM).

Table 5
Compactness

IAU Name (1)	ν (GHz) (2)	S_{tot} (Jy) (3)	S_{core} (Jy) (4)	S_{core}/S_{tot} (5)	S_s (Jy) (6)	S_l (Jy) (7)	S_l/S_s (8)
0202+319	43	1.04	0.80	0.79	1.04 ± 0.04	0.41 ± 0.04	0.39
	86	0.32	0.29	0.94	0.30 ± 0.08	0.26 ± 0.05	0.87
0529+483	43	0.35	0.30	0.87	0.35 ± 0.05	0.18 ± 0.03	0.51
	86	0.26	0.26	1.00	0.26 ± 0.04	0.21 ± 0.03	0.81
1030+415	43	0.68	0.44	0.64	0.69 ± 0.06	0.39 ± 0.06	0.57
	86	0.26	0.20	0.77	0.24 ± 0.08	0.16 ± 0.05	0.67
1128+385	43	0.72	0.53	0.73	0.72 ± 0.04	0.37 ± 0.08	0.51
	86	0.18	0.17	1.00	0.17 ± 0.07	0.17 ± 0.06	1.00
1418+546	43	1.30	0.83	0.64	1.28 ± 0.05	0.53 ± 0.08	0.41
	86	0.31	0.24	0.77	0.30 ± 0.12	0.19 ± 0.07	0.63
1823+568	43	0.65	0.46	0.71	0.63 ± 0.03	0.33 ± 0.04	0.52
	86	0.24	0.23	0.92	0.24 ± 0.09	0.23 ± 0.06	0.96
1828+487	43	1.13	0.90	0.79	1.10 ± 0.12	0.46 ± 0.09	0.42
	86	0.27	0.25	0.93	0.25 ± 0.07	0.21 ± 0.06	0.84
1928+738	43	3.88	3.31	0.85	3.95 ± 0.11	2.15 ± 0.18	0.54
	86	0.23	0.21	0.88	0.24 ± 0.10	0.21 ± 0.04	0.88
1954+513	43	0.71	0.50	0.70	0.64 ± 0.02	0.43 ± 0.04	0.67
	86	0.17	0.17	1.00	0.20 ± 0.10	0.18 ± 0.09	0.90
2201+315	43	1.21	0.80	0.66	1.16 ± 0.04	0.52 ± 0.08	0.45
	86	0.53	0.33	0.62	0.41 ± 0.19	0.21 ± 0.05	0.51

Note. (1) Source name (B1950.0); (2) observing frequency; (3) integrated flux density; (4) core flux density; (5) ratio of the core flux density to the total integrated flux density; (6) correlated flux density on the shortest baseline; (7) correlated flux density on the longest baseline projected in the position angle perpendicular to the jet direction; (8) ratio of the correlated flux density on the longest baseline to the shortest baseline.

the quiescent phase, which can be seen from the OVRO 40 m 15 GHz light curve monitoring program (Richards et al. 2011).

3.4.9. 1954+513 (J1955+5131)

The source 1954+513 (OV 591) is a radio-loud quasar with a redshift of $z = 1.22$ and was detected with a fractional linear optical polarization below 3% (Lawrence et al. 1996; Véron-Cetty & Véron 2010). Neither EGRET nor *Fermi*/LAT have detected this source. Perley (1982) reported a classical core–double-lobe FR II structure oriented in the north–south direction with a total extent of 16″ (130 kpc). The northern lobe has a trailing jet continuously connected with the core, in which a midway hotspot is seen at about 5″ from the core. The naturally weighted 5 GHz VLA image shows that the southern component is slightly elongated toward the core, but there is no evidence of a counter-jet (Kollgaard et al. 1990). The images acquired by VSOP and the VLBA at 5 GHz (Dodson et al. 2008) showed a compact core and a faint extended component at a position angle $-27°$ separated by 0.4 mas with a flux density about 230 mJy, exceeding 60% of the flux density resolved with space–ground baselines (Lister et al. 2001).

The 2.3 GHz and 15 GHz VLBI images (Figures 10(a)–(b)) revealed a rich jet structure ∼50 mas to the northwest of the core (Kovalev et al. 2005; Pushkarev & Kovalev 2012). Our new 43 GHz image (Figure 10(c)) resolved the inner 2 mas jet into a series of five components that follow a straight trajectory along a P.A. of $-55°$ until 1.3 mas, where the jet bends into a jet component J2 at a position angle of $-68°$. By comparing with the 15 GHz image, we find that the jet turns back to a position angle of $-50°$ after the jet component J1, where polarized emission was detected (Lister et al. 2009). Enhanced polarized emission at the bending location probably implies a local interaction between the jet and a massive cloud in the

narrow-line region of the host galaxy. Such jet–cloud interaction may deflect the jet flow and alter its direction.

The snapshot 86 GHz image detected a naked core with a flux density about 275 mJy (Lee et al. 2008). The core is also unresolved in our new 86 GHz image (Figure 10(d)), with a flux density about 170 mJy. The core flux densities at the two epochs differ by 100 mJy. The peak specific intensity of the inner jet J5 in the 43 GHz image is 26 mJy beam^{-1}. Considering the steep-spectrum nature of the jet, its expected peak specific density at 86 GHz is below the detection threshold, i.e., five times the rms noise of the 86 GHz image (1σ = 2.9 mJy beam^{-1}).

3.4.10. 2201+315 (J2203+3145)

2201+315 (4C +31.63) at a redshift of $z = 0.2974$ was identified as a low optical polarization quasar (Marziani et al. 1996) and an intermediate-spectral-peaked source (Véron-Cetty & Véron 2010). It was detected by the *Fermi*/LAT with a 5σ significance (Acero et al. 2015). It is also a strong X-ray AGN observed by *Swift* with a flux of 3.22×10^{-12} erg cm^{-2} s^{-1} at $0.1-2.4$ keV (Maselli et al. 2010). The optical image shows signs of a post-merger with an unusual distribution of dust (Hutchings et al. 1984). In the radio band, this quasar displays a typical FR II morphology with a total size of ∼90″ with a bright core and double lobes at opposite sides of the core aligning in the northeast–southwest direction (Gower & Hutchings 1984; Neff & Brown 1984; Cooper et al. 2007). The southwestern lobe is linked to the core with an extended jet. The counter-jet was not detected in the VLA images.

In the 1.4 GHz VLBA image, the southwest jet was observed to extend up to a distance of 90 mas (Figure 11(a)). At higher frequencies of 8.6 and 15 GHz (Figure 11(b)), the jet shows a smooth bending from a position angle of $-150°$ to $-130°$ (Kellermann et al. 2004). Superluminal motions have been

Table 6
Derived Parameters of VLBI Cores

IAU Name (1)	Epoch (2)	ν (GHz) (3)	S_{core} (Jy) (4)	$\alpha_{8.1-15.4}$ (5)	α_{22-94} (6)	T_b (10^{10} K) (7)
0202+319	2014 Nov 21	43	0.80	−0.46	−0.4	17.2
	2014 Nov 30	86	0.29			1.8
0529+483	2014 Nov 21	43	0.32	0.04	−0.1	4.6
	2014 Nov 30	86	0.26			1.5
1030+415	2015 Mar 08	43	0.46	⋯	−0.3	14.6
	2014 Nov 29	86	0.20			1.9
1128+385	2015 Mar 08	43	0.51	⋯	−0.4	36.9
	2014 Nov 29	86	0.17			8.5
1418+546	2015 Mar 08	43	0.86	−0.12	0.2	11.7
	2014 Nov 29	86	0.24			0.4
1823+568	2015 Jan 10	43	0.45	−0.32	−0.4	17.7
	2016 May 06	86	0.23			2.5
1828+487	2015 Jan 10	43	0.79	−0.61	−0.3	19.6
	2016 May 06	86	0.22			15.4
1928+738	2015 Jan 10	43	3.75	−0.51	−0.3	23.7
	2016 May 06	86	0.21			5.6
1954+513	2015 Jan 10	43	0.52	⋯	−0.1	19.0
	2016 May 06	86	0.17			1.0
2201+315	2015 Jan 10	43	1.06	−0.32	−0.4	3.4
	2016 May 06	86	0.33			0.9

Note. (1) Source name (B1950.0); (2) observing epoch; (3) observing frequency; (4) total flux density of the core; (5) brightness temperature.

detected in seven jet components with a maximum value of 0.45 mas yr^{-1} (8.3 ± 0.1c) (Lister et al. 2013). The published 86 GHz image (Lee et al. 2008) only detected the central core.

Our 43 and 86 GHz observations (Figures 11(c)–(d)) show the jet structure within 2 mas, in which three jet components are identified. The images at two frequencies are in excellent agreement, revealing the initial section of the jet along a P.A. ∼−160°. In combination with the outer mas-scale jet and more extended arcsec-scale jets/lobes, our new images reinforce that the jet has a smooth bending trajectory; the position angle gradually changes from −166° (at ⩽1 mas) to −130° (1–90 mas), and ends in a terminal shock at a P.A. = −120° (at 13″).

4. Summary

We have observed 10 radio-loud AGNs with the VLBA at 43 and 86 GHz, and have examined the inner jet morphologies. The highest resolution is 0.18 mas and the typical noise level in the high-sensitivity images is 0.3 mJy beam^{-1} at 43 GHz (natural weighting). The highest resolution at 86 GHz is 0.07 mas, and the noise level is 1.5 mJy beam^{-1} with uniform weighting and 1.0 mJy beam^{-1} with natural weighting. These sources are the brightest radio QSOs selected from our large sample (including a total of 134 AGNs) for the purpose of high-frequency VLBA imaging surveys. The present paper focuses on presenting the sub-mas-scale jet structure. The main results are summarized as follows.

1. The VLBA images of nine sources (except 1928+738) at 43 GHz and of two sources (0202+319, 0529+483) at 86 GHz are presented for the first time. For another eight sources, our 86 GHz images have a substantially better sensitivity than the previous ones obtained from snapshot observations.
2. Seven sources show core–jet structure at 86 GHz, and three others (0529+483, 1128+385 and 1954+513)

show an unresolved core at 86 GHz. We detect seven new components in 43 GHz images within 0.8 mas of the core, and three new components at 86 GHz within 0.5 mas.

3. All sources show a resolved core–jet morphology at 43 GHz. A majority of the sources show that the core dominates more than 70% of the total flux density at 43 GHz, except for 1030+415 (helical jet), 1418+546, 2201+315 (an FR II source). The high core dominance detected at 43 and 86 GHz confirms that they can be good phase calibrators for ground-based mm-VLBI experiments and for future space mm/submm-wavelength VLBI.
4. Three sources (0202+319, 1030+415, 1928+738) display helically twisted jets on parsec scales. The jets in other sources show a straight trajectory. In these three sources, the jet shows a large misalignment between the mas and arcsecond scales: in 1030+415, the 43 and 86 GHz observations have revealed a substantially different inner jet position angle than what is seen at 2.3 GHz (i.e., a sharply curved jet); in 1418+546, the mas-scale jet points to the southeast, but the VLA image shows a western lobe; in 1823+568, the mas-scale VLBI jet extends to the southwest, while the arcsecond-scale jet in the VLA image points to the east. The large misalignment of the jet direction warrants further detailed study.
5. Nine sources have T_b higher than 10^{11} K at 43 GHz, indicating a highly beamed jet. The core brightness temperatures derived at 43 GHz are systematically higher than those at 86 GHz. A detailed discussion of the statistical properties, including the brightness temperature of the core, source compactness, and other jet parameters, will be given in a following paper.
6. 1418+546 is observed with 86 GHz VLBI with a core flux density of 0.24 Jy. Due to its high flux density, compact structure, and slowly varying structure, it can be used as a

ORCID iDs

X.-P. Cheng ⓘ https://orcid.org/0000-0003-4407-9868
T. An ⓘ https://orcid.org/0000-0003-4341-0029
J. Yang ⓘ https://orcid.org/0000-0002-2322-5232
P. Mohan ⓘ https://orcid.org/0000-0002-2211-0660
K. I. Kellermann ⓘ https://orcid.org/0000-0002-0093-4917
M. L. Lister ⓘ https://orcid.org/0000-0003-1315-3412
S. Frey ⓘ https://orcid.org/0000-0003-3079-1889
X.-F. Li ⓘ https://orcid.org/0000-0002-9093-6296

References

Abdo, A. A., Ackermann, M., Ajello, M., et al. 2010, ApJ, 188, 405
Acero, F., Ackermann, M., Ajello, M., et al. 2015, ApJ, 218, 23
An, T., Baan, W. A., Wang, J.-Y., Wang, Y., & Hong, X.-Y. 2013, MNRAS, 434, 3487
An, T., Hong, X. Y., Hardcastle, M. J., et al. 2010, MNRAS, 402, 87
An, T., Wu, X., & Frey, S. 2014, Ap&SS, 352, 825 (Paper I)
Beasley, A. J., Dhawan, V., Doeleman, S., & Phillips, R. B. 1997, in Millimeter-VLBI Science Workshop, ed. R. Barvainis & R. B. Phillips (Cambridge, MA: MIT), 53
Beasley, A. J., Gordon, D., Peck, A. B., et al. 2002, ApJ, 141, 13
Burbidge, E. M. 1970, ApJL, 160, L33
Burke, B. F. 1984, in IAU Symp. 110, VLBI and Compact Radio Sources, ed. R. Fanti, K. Kellermann, & G. Setti (Dordrecht: Reidel), 397
Camenzind, M. 1986, A&A, 156, 137
Camenzind, M., & Krockenberger, M. 1992, A&A, 255, 59
Cassaro, P., Stanghellini, C., Bondi, M., et al. 1999, A&AS, 139, 601
Chatterjee, R., Marscher, A. P., Jorstad, S. G., et al. 2009, ApJ, 704, 1689
Chen, X., Rachen, J. P., López-Caniego, M., et al. 2013, A&A, 553, A107
Chen, X., & Wright, E. L. 2009, ApJ, 694, 222
Cooper, N. J., Lister, M. L., & Kochanczyk, M. D. 2007, ApJ, 171, 376
Deller, A. T., Brisken, W. F., Phillips, C. J., et al. 2011, PASP, 123, 275
Deller, A. T., Tingay, S. J., Bailes, M., & West, C. 2007, PASP, 119, 318
Dodson, R., Fomalont, E. B., Wiik, K., et al. 2008, ApJ, 175, 314
Doeleman, S., Agol, E., Backer, D., et al. 2009, arXiv:0906.3899
Doeleman, S. S., Fish, V. L., Schenck, D. E., et al. 2012, Sci, 338, 355
Fanti, C., Fanti, R., Parma, P., Schilizzi, R. T., & van Breugel, W. J. M. 1985, A&A, 143, 292
Feng, W. X., An, T., Hong, X. Y., et al. 2005, A&A, 434, 101
Fey, A. L., Ma, C., Arias, E. F., et al. 2004, AJ, 127, 3587
Gabuzda, D. C., & Cawthorne, T. V. 1996, MNRAS, 283, 759
Geréb, K., & Frey, S. 2011, AdSpR, 48, 334
Gold, B., Odegard, N., Weiland, J. L., et al. 2011, ApJ, 192, 15
Gower, A. C., & Hutchings, J. B. 1984, AJ, 89, 1658
Gregory, P. C., Scott, W. K., Douglas, K., & Condon, J. J. 1996, ApJ, 103, 427
Greisen, E. W. 2003, in Information Handling in Astronomy—Historical Vistas, Vol. 285, ed. A. Heck (Dordrecht: Springer), 109
Hardee, P. E. 2003, ApJ, 597, 798
Healey, S. E., Romani, R. W., Taylor, G. B., et al. 2007, ApJ, 171, 61
Helmboldt, J. F., Taylor, G. B., Tremblay, S., et al. 2007, ApJ, 658, 203
Hewett, P. C., & Wild, V. 2010, MNRAS, 405, 2302
Hirabayashi, H., Hirosawa, H., Kobayashi, H., et al. 1998, Sci, 281, 1825
Hodgson, J. A., Krichbaum, T. P., Marscher, A. P., et al. 2017, A&A, 597, A80
Hong, X., Shen, Z., An, T., & Liu, Q. 2014, AcAau, 102, 217
Hovatta, T., Aller, M. F., Aller, H. D., et al. 2014, AJ, 147, 143
Hutchings, J. B., Crampton, D., Campbell, B., Duncan, D., & Glendenning, B. 1984, ApJ, 55, 319
Johnston, K. J., Simon, R. S., Eckart, A., et al. 1987, ApJL, 313, L85
Kardashev, N. S., Khartov, V. V., Abramov, V. V., et al. 2013, ARep, 57, 153
Kellermann, K. I., Lister, M. L., Homan, D. C., et al. 2004, ApJ, 609, 539
Kellermann, K. I., & Pauliny-Toth, I. I. K. 1969, ApJL, 155, L71
Kollgaard, R. I., Wardle, J. F. C., & Roberts, D. H. 1990, AJ, 100, 1057
Kollgaard, R. I., Wardle, J. F. C., Roberts, D. H., & Gabuzda, D. C. 1992, AJ, 104, 1687
Komissarov, S. S., Barkov, M. V., Vlahakis, N., & Königl, A. 2007, MNRAS, 380, 51
Kovalev, Y. Y., Kellermann, K. I., Lister, M. L., et al. 2005, AJ, 130, 2473
Koyama, S., Kino, M., Nagai, H., et al. 2013, PASJ, 65, 29
Krichbaum, T. P., & Witzel, A. 1992, in Variability of Blazars, ed. E. Valtaoja & M. Valtonen (Cambridge: Cambridge Univ. Press), 205
Kun, E., Gabányi, K. É, Karouzos, M., Britzen, S., & Gergely, L. Á 2014, MNRAS, 445, 1370
Lanyi, G. E., Boboltz, D. A., Charlot, P., et al. 2010, AJ, 139, 1695
Laurent-Muehleisen, S. A., Kollgaard, R. I., Ryan, P. J., et al. 1997, A&AS, 122, 235
Lawrence, C. R., Pearson, T. J., Readhead, A. C. S., & Unwin, S. C. 1986, AJ, 91, 494
Lawrence, C. R., Zucker, J. R., Readhead, A. C. S., et al. 1996, ApJ, 107, 541
Lee, S.-S., Lobanov, A. P., Krichbaum, T. P., et al. 2008, AJ, 136, 159
Lee, S.-S., Wajima, K., Algaba, J.-C., et al. 2016, ApJS, 227, 8
Linfield, R. 1981, ApJ, 250, 464
Linford, J. D., Taylor, G. B., Romani, R. W., et al. 2012, ApJ, 744, 177
Lister, M. L. 2001, ApJ, 562, 208
Lister, M. L., Aller, H. D., Aller, M. F., et al. 2009, AJ, 137, 3718
Lister, M. L., Aller, M. F., Aller, H. D., et al. 2013, AJ, 146, 120
Lister, M. L., Aller, M. F., Aller, H. D., et al. 2016, AJ, 152, 12
Lister, M. L., Tingay, S. J., Murphy, D. W., et al. 2001, ApJ, 554, 948
Lobanov, A. P., Krichbaum, T. P., Graham, D. A., et al. 2000, A&A, 364, 391
Lonsdale, C. J., Doeleman, S. S., & Phillips, R. B. 1998, AJ, 116, 8
Ma, C., Arias, F. E., Bianco, G., et al. 2013, yCat, 1323, 0
Marscher, A. P., Jorstad, S. G., Mattox, J. R., & Wehrle, A. E. 2002, ApJ, 577, 85
Marziani, P., Sulentic, J. W., Dultzin-Hacyan, D., Calvani, M., & Moles, M. 1996, ApJ, 104, 37
Maselli, A., Cusumano, G., Massaro, E., et al. 2010, A&A, 520, A47
McKinney, J. C., Tchekhovskoy, A., & Blandford, R. D. 2012, MNRAS, 423, 3083
Mohan, P., & Mangalam, A. 2015, ApJ, 805, 91
Murphy, D. W., Browne, I. W. A., & Perley, R. A. 1993, MNRAS, 264, 298
Narayan, R. 2005, NJPh, 7, 199
Neff, S. G., & Brown, R. L. 1984, AJ, 89, 195
Niinuma, K., Lee, S.-S., Kino, M., et al. 2014, PASJ, 66, 103
Nolan, P. L., Abdo, A. A., Ackermann, M., et al. 2012, ApJ, 199, 31
Pearson, T. J., & Readhead, A. C. S. 1988, ApJ, 328, 114

Perley, R. A. 1982, AJ, 87, 859
Petrov, L., Kovalev, Y. Y., Fomalont, E. B., & Gordon, D. 2008, AJ, 136, 580
Petrov, L., Lee, S.-S., Kim, J., et al. 2012, AJ, 144, 150
Planck Collaboration, Ade, P. A. R., Aghanim, N., et al. 2011, A&A, 536, A7
Plotkin, R. M., Miller-Jones, J. C. A., Gallo, E., et al. 2017, ApJ, 834, 104
Polatidis, A. G., Wilkinson, P. N., Xu, W., et al. 1995, ApJ, 98, 1
Pushkarev, A. B., & Kovalev, Y. Y. 2012, A&A, 544, A34
Rantakyrö, F. T., Bååth, L. B., Backer, D. C., et al. 1998, A&AS, 131, 451
Readhead, A. C. S., Mason, C. R., Mofett, A. T., et al. 1983, Natur, 303, 504
Richards, J. L., Max-Moerbeck, W., Pavlidou, V., et al. 2011, ApJ, 194, 29
Rusk, R., & Rusk, A. C. M. 1986, CaJPh, 64, 440
Schneider, D. P., Hall, P. B., Richards, G. T., et al. 2007, AJ, 134, 102
Shaw, M. S., Romani, R. W., Cotter, G., et al. 2012, ApJ, 748, 49
Shepherd, M. C. 1997, adass VI, 125, 77
Stirling, A. M., Cawthorne, T. V., Stevens, J. A., et al. 2003, MNRAS, 341, 405
Tchekhovskoy, A., McKinney, J. C., & Narayan, R. 2012, JPhCS, 372, 012040
Véron-Cetty, M.-P., & Véron, P. 2006, A&A, 455, 773
Véron-Cetty, M.-P., & Véron, P. 2010, A&A, 518, A10
Wang, J.-Y., An, T., Baan, W. A., & Lu, X.-L. 2014, MNRAS, 443, 58
White, R. L., Becker, R. H., Helfand, D. J., & Gregg, M. D. 1997, ApJ, 475, 479
Wilkinson, P. N., Booth, R. S., Cornwell, T. J., & Clark, R. R. 1984, Natur, 308, 619
Wilkinson, P. N., Tzioumis, A. K., Benson, J. M., et al. 1991, Natur, 352, 313
Xu, W., Readhead, A. C. S., Pearson, T. J., Polatidis, A. G., & Wilkinson, P. N. 1995, ApJ, 99, 297
Zhao, W., Hong, X.-Y., An, T., et al. 2011, A&A, 529, A113